Theses and Dissertations

Student Graduate Works

3-22-2019

Comparing Dual-Polarization Radar Lightning Forecast Methods across Southwest Utah

Daniel O. Katuzienski

**Comparing Dual-Polarization Radar Lightning
Forecast Methods Across Southwest Utah**

THESIS

Daniel O. Katuzienski, 1st Lt, USAF

AFIT-ENP-MS-19-M-083

**DEPARTMENT OF THE AIR FORCE
AIR UNIVERSITY**

AIR FORCE INSTITUTE OF TECHNOLOGY

Wright-Patterson Air Force Base, Ohio

DISTRIBUTION STATEMENT A
APPROVED FOR PUBLIC RELEASE; DISTRIBUTION UNLIMITED.

The views expressed in this document are those of the author and do not reflect the official policy or position of the United States Air Force, the United States Department of Defense or the United States Government. This material is declared a work of the U.S. Government and is not subject to copyright protection in the United States.

AFIT-ENP-MS-19-M-083

COMPARING DUAL-POLARIZATION RADAR

LIGHTNING FORECAST METHODS

ACROSS SOUTHWEST UTAH

THESIS

Presented to the Faculty

Department of Engineering Physics

Graduate School of Engineering and Management

Air Force Institute of Technology

Air University

Air Education and Training Command

in Partial Fulfillment of the Requirements for the

Degree of Master of Science in Atmospheric Science

Daniel O. Katuzienski, B.S.

1st Lt, USAF

21 Mar 2019

AFIT-ENP-MS-19-M-083

COMPARING DUAL-POLARIZATION RADAR

LIGHTNING FORECAST METHODS

ACROSS SOUTHWEST UTAH

THESIS

Daniel O. Katuzienski, B.S.
1st Lt, USAF

Committee Membership:

Maj O. Nava, Ph.D., USAF
Chair

Maj C. Lewis, Ph.D., USAF
Member

Capt N. Zimmerman, M.S., USAF
Member

Abstract

Lightning poses a significant hazard to space launch operations to include ground processing, launch window forecasts, and rocket-triggered lightning events. Two lightning initiation forecast methods using weather radar developed in Gremillion and Orville (1999) and Travis (2015) for Cape Canaveral Air Force Station (CCAFS) and Kennedy Space Center (KSC), Florida are tested in a new geographical region. This is accomplished by applying the highest-performing radar parameters from Gremillion and Orville (1999): reflectivity (Z) $\geq$ 40 dBZ for two consecutive volume scans at the $-10°C$ thermal height and Travis (2015): $Z \geq 36.5$ dBZ with differential reflectivity (Z_{DR}) $\geq$ 0.31 dB at the $-10°C$ thermal height, across southwest Utah's multi-dimensional lightning detection network, the Telescope Array Lightning Mapping Array (TA LMA). Both methods are tested on 102 isolated, warm-season thunderstorms between August 2015 and August 2018. A follow-up study Olsen (2018) was conducted in the Washington, D.C. area using Travis' parameters, where poor performance was recorded. Forecast metrics and lead times are calculated and compared to the results of Gremillion and Orville (1999), Travis (2015), and Olsen (2018). The findings of this study confirm that the lightning prediction methods from both studies do not function well for Utah. Despite being tested in different climates, the forecast lead times of all three study locations are statistically significant. Additional results also conclude that Z is the determining factor within Utah lightning initiation prediction algorithms and that Z_{DR} lightning prediction is not geographically robust.

iv

Acknowledgements

It would have been impossible to complete AFIT without the love and support from my wife. You have always been my biggest supporter, and a constant source of positive and constructive feedback. I look forward to spending more time together in Florida, and all the new exciting challenges that lay ahead of us in this next chapter. Also, to my Dad and brother, who served as my terrific editors...you were both a huge help to me. Thanks for your hours of time and assistance in the writing process.

I would also like to thank my academic advisor, Maj Omar Nava, for always challenging me academically and forcing me to be a better writer. I have no doubt that these skills you have taught me will help me immensely in my future. Your time and efforts has enabled me to think more critically, and solve problems I would have previously thought impossible. This has ultimately made me a better USAF officer.

Also, thank you to Lt Mason Sorrell of Virginia Tech AFROTC Detachment 875. The nearly three weeks of your summer that you sacrificed has made this study possible. I am also grateful to Mr. Jeff Zautner, of the 14th Weather Squadron. Thank you for your apt support to my climatology request and the time/efforts you set aside for this project. Last, but not certainly not least, thank you to Dr. William Rison of New Mexico Tech. The lightning data you have provided me with has made this research possible, and I am eternally grateful for your generosity and assistance.

Daniel O. Katuzienski

Table of Contents

List of Figures

List of Tables

List of Acronyms

45 SW 45th Space Wing

45 WS 45th Weather Squadron

4DLSS Four Dimensional Lightning Surveillance System

AFB Air Force Base

AFMAN Air Force Manual

AI Artificial Intelligence

AOR Area of Responsibility

ASOS Automated Surface Observing Systems

CA Cloud-to-Air

CC Cloud-to-Cloud

CCAFS Cape Canaveral Air Force Station

CG Cloud-to-Ground

CI Confidence Interval

CR Correct Rejection

CSI Critical Success Index

DNE Does Not Exist

DoD Department of Defense

DoL Department of Labor

DP Dual-Polarization

EM Electromagnetic Radiation

FA False Alarm

FAA Federal Aviation Administration

FAR False Alarm Rate

GLM Geostationary Lightning Mapper

GOES Geostationary Operational Environmental Satellite

GR2Analyst Gibson Ridge 2 Analyst$^{\text{TM}}$ Software

IC Intracloud

IEM Iowa Environmental Mesonet

KICX Cedar City Radar

KMTX Salt Lake City Radar

KSC Kennedy Space Center

LDAR Lightning Detection and Ranging

LIST Lightning Initiation Signature

LLWAS Low Level Wind Shear Alert System

LMA Lightning Mapping Array

MSL Mean Sea Level

NASA National Aeronautics and Space Administration

NCEI National Centers for Environmental Information

NEXRAD Next-Generation Radar

NLDN National Lightning Detection Network

NLSI National Lightning Safety Institute

NMT New Mexico Institute of Mining and Technology

NOAA National Oceanic and Atmospheric Association

NWS National Weather Service

OCDS Operational Climatic Data Summary

PFA Probability of False Alarms

POD Probability of Detection

PRF Pulse Repetition Frequency

TA Telescope Array

TOA Time-of-Arrival

TSS True Skill Statistic

USAF United States Air Force

VCP Volume Coverage Pattern

VHF Very High Frequency

WS Weather Squadron

WSR-88D Weather Surveillance Radars-1988 Doppler

I. Introduction

1.1 Motivation

In the United States, annual lightning costs and losses exceed \$5 to \$6 billion (NLSI, 2018). Lightning has tremendous economic impacts on insurance, mining, petrochemical, and electrical industries. Notwithstanding direct damage, the loss in time and resources and the disruption of operations at commercial airports, public areas, and the Department of Defense (DoD) facilities due to lightning is incalculable. For instance, United States Air Force (USAF) weather guidance, Air Force Manual (AFMAN) 15-111, requires that a thunderstorm shall be reported at a location for 15 min after the last lightning strike occurred. This 15 min is time lost in aircraft launch and recovery operations when lightning may no longer be a threat. In addition to costly and time-related impacts, in years that do not include Hurricane Andrew (1992), lightning is ranked second in the annual number of deaths among natural disasters across the country (Cooper, 1995). For example, the United States Bureau of Labor (U.S. DoL, 2018) reports that an average of 82 people die each year from lightning strikes, with southern states reporting the highest numbers. Consequently, much research is dedicated to the improvement of lightning-related weather forecasts. One such USAF organization particularly interested in improved lightning initiation forecasts is the 45th Weather Squadron (45 WS), which is responsible for supporting space launch operations in Florida at Cape Canaveral Air Force Station (CCAFS), Kennedy Space Center (KSC), and Patrick Air Force Base (AFB). The squadron is also tasked with safeguarding 25,000 personnel and providing resource protection for over \$20 billion in equipment and facilities within the aerodrome (Roeder, 2018).

CCAFS/KSC is America's gateway for manned spaceflight, with launch operators including the National Aeronautics and Space Administration (NASA), DoD, USAF,

and various commercial corporations. Lightning causes significant delays in launch preparation efforts due to its impact on ground operations. Ground delays for the crews who are readying space vehicles for launch are caused by lightning watches and warnings issued by the 45 WS, which halts operations until the lightning threat ends (Roeder, 2018). Continuous interruptions during this critical launch preparation phase can jeopardize long and short-term launch schedules. In addition, lightning can be a factor during the launch window due to the threat of natural and rocket-triggered lightning. Triggered lightning events occur when a rocket passes through a strong pre-existing electric field (Roeder, 2018). Facility upgrades in recent years to include dual-polarization (DP) weather radar and multi-dimensional lightning detection equipment have improved lightning forecasts, but the 45 WS still retains a high false alarm rate.

The possible return of manned space flight, coupled with a projected increase in the number of future launches, requires that weather forecasts be more accurate than ever before. New launch initiatives brought on by the 45th Space Wing (45 SW) at Patrick AFB and CCAFS/KSC strive for an unprecedented 48 per year launch manifest (45 SW, 2017). Improving upon lightning forecasts for the 45 SW is a critical component in reducing the overreaching impact weather has on launch efforts. Accurate lightning forecasts using DP weather radar offers a potential solution. Meeting this intent will ensure that the core mission of the Wing is bold, flexible, and creative.

1.2 Research Objective

The application of traditional (non-DP) and DP radar lightning initiation signatures in a climate different to that of the area for which it was developed is a challenging problem that requires more research. The purpose of this study is to verify two lightning initiation forecast methods developed by the Air Force Institute of Technology for the CCAFS/KSC area in Gremillion and Orville (1999) and Travis

(2015). This is accomplished by applying the highest performing lightning initiation radar parameters to the Utah area and comparing the forecast metrics and lead times from the two methods. The results of the Utah dataset are then compared to a similar study (Olsen, 2018) which applied Travis' radar parameters to lightning forecasts across the Washington, D.C. area. Olsen found that Travis' method did not perform well for the new area, resulting in too many false alarms. The negative results of the Washington, D.C. study suggested research be conducted in a new region to confirm the results and draw new conclusions about the spatial behavior of radar parameters.

Utah is the ideal test site because of the significant elevation and climate differences of Florida and Washington, D.C. In addition, Utah also has a multi-dimensional lightning detection network similar to the system at CCAFS/KSC, which was used in Travis (2015). The lightning data is provided at no-cost courtesy of the New Mexico Institute of Mining and Technology (NMT). The weather in Utah also makes it the perfect location to study lightning, as airmass thunderstorms are the dominant type of thunderstorms in this area and are one of the main requirements of the two forecast methods. Lastly, by testing the technique from Gremillion and Orville (1999), which uses only traditional (i.e. non-DP) radar parameters, this study allows for a measure of forecast skill using DP variables in radar lightning forecast methods.

1.3 Preview

Chapter I introduces the motivation for this study, the scope of the problem, and the research objective. Chapter II provides a background of several topics applicable to the research, to include instrumentation and aspects related to lightning initiation. Chapter III describes the methodology used to manipulate the lightning and radar data. Chapter IV details data analysis and research results. Chapter V discusses conclusions and recommendations for future work.

II. Background

2.1 Lightning

This section details the thunderstorm charging and lightning discharge mechanisms. Lightning is described as a transient, high-current electric discharge that results from charge separation within thunderstorms (Uman, 2001). It occurs either cloud-to-ground (CG), cloud-to-cloud (CC), intra-cloud (IC), or cloud-to-air (CA). Lightning is produced through cloud electrification and lightning discharge processes.

2.1.1 Cloud Electrification

Cloud electrification is the charging process that occurs within a thunderstorm before lightning discharge. This electrification occurs as a result from the combination of several different charging mechanisms: drop break-up, ion charging, convective charge transport, inductive, and non-inductive processes (Saunders, 2008). Non-inductive processes are accepted as the dominant electrification mechanisms within airmass thunderstorms and are the focus of this study. This is due to the relatively short period of time required by this charging process in order to induce the level of electrification necessary to produce lightning discharge (Takahashi, 1978).

Non-inductive charging, also known as ice/graupel charging, was first discovered in laboratory experiments conducted by Reynolds et al. (1957). The research found a charge transfer occurs when ice crystals collide and coalesce with riming graupel particles and that the ice removes the equal and opposite charge of the graupel. Figure 1 shows this collision process consisting of graupel, ice crystals, and supercooled water droplets within a thunderstorm. The results described this as the primary reason why larger/heavier negatively-charged regions of graupel exist within the lower portion of thunderstorms and why lighter positively-charged particles are carried aloft into the

4
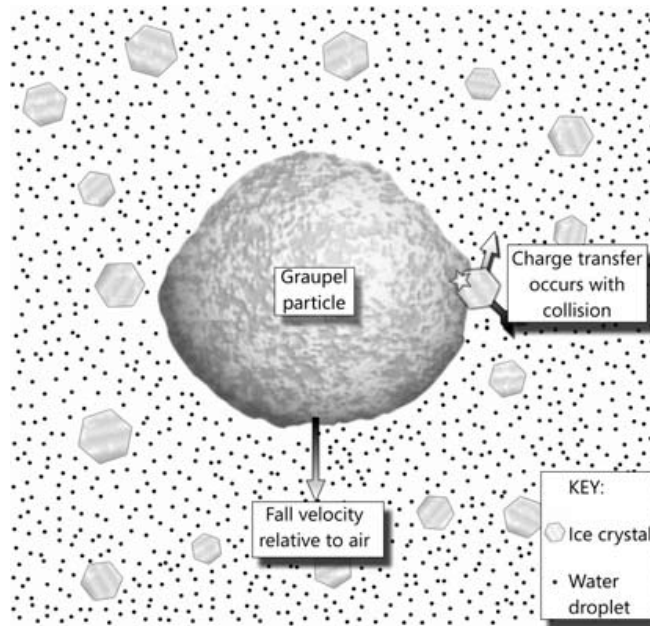
Figure 1. Schematic of a graupel particle showing the interaction with ice crystals and suspended water droplets within the mixed-phase region of a thunderstorm. Adapted from Emersic (2006).

upper-regions of thunderstorms. Saunders (2008) further described the accretion process of suspended water droplets onto ice crystals as a necessary component in cloud electrification. This is because the water droplets allow for larger and negatively-charged cloud-spectra to collide with graupel particles within the mixed-phase region.

Observed thunderstorm charging requirements are detailed within Mason (1953). The main negative charging center is between the $-5°C$ and $-25°C$ thermal levels, with the main positive center a few kilometers above the negative center. Mason found that the charging mechanism must generate 5 to 30 C km^{-3} leading to a charge generation rate of order 1 C km^{-3} min^{-1}. Subsequent research indicated that the size of the individual droplets is also an important component in the charging process. Avila et al. (1999) found that larger cloud-droplet spectra correlate with the sign of the electric charge transferred. In general, the larger the cloud-droplets, the more negative the graupel/hailstones are and the stronger the resultant thunderstorm.

2.1.2 Lightning Discharge

Lightning strikes occur when enough oppositely-charged graupel and ice particles are separated throughout the cloud (Reynolds et al., 1957). If enough charges are separated, the electric field intensifies to the point of dielectric breakdown, which exceeds the critical value of air electric field suppression (Wallace and Hobbs, 2006). The required level of electric field intensity for lightning initiation is 3×10^6 V m^{-1} (Rakov and Uman, 2003). This critical value is only valid for dry air at sea level pressure, as the presence of hydrometeors and lower air pressure decreases the required electric field intensity. For example, at an altitude of 6 km with the presence of > 1.4 mm diameter water droplets, the electric field level required for a strike decreases to 1×10^6 V m^{-1} (Rakov and Uman, 2003).

Lightning flashes consist of the initial dielectric breakdown, followed by a stepped leader and a return stroke. Stepped leaders last for $6-8\mu$s (Krider et al., 1977), while return strokes occur for several seconds. The resulting flash of lightning persists until no potential electric difference remains. Similarly, return strokes remain visible as long as there is a flow of electrons between two opposing charge regions. Lightning discharges occur either between the charge regions (IC/CC/CA lightning) or between a charge region and the ground (CG lightning). The cloud electrification and charging mechanisms preceding a lightning strike can be detected using weather radar.

2.2 Weather Radar

This section describes one of two meteorological tools utilized within this study to interrogate thunderstorms. It also provides insight into the differences between DP and non-DP weather radar and the two radar products used within this research.

The first use of radar for meteorological purposes can be traced back to World War II, when British scientists experimented with 10 cm wavelength radars in order to
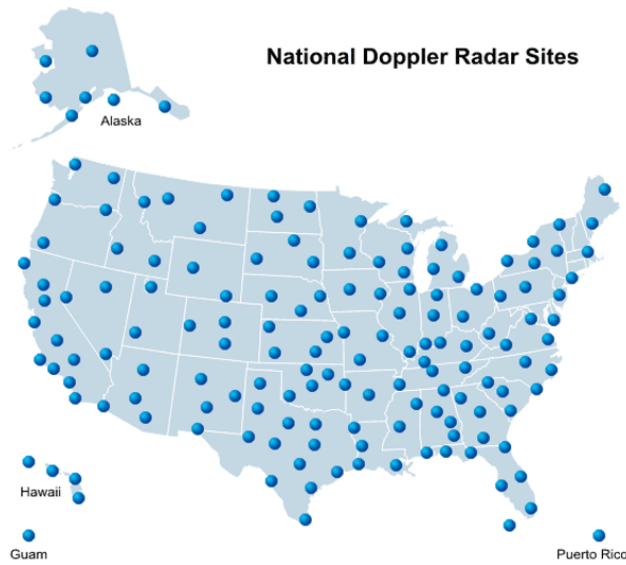
Figure 2. A map of the 159 WSR-88D sites across the United States and at DoD installations around the world. Adapted from NWS (2018).

detect enemy airplanes during the height of the Battle of Britain (Whiton et al., 1998). False airplane echoes seen on radar caused by weather phenomena prompted post-war research efforts in order to investigate what was causing these effects. American scientists at the Massachusetts Institute of Technology's (MIT) Radiation Laboratory were the first to confirm that certain types of radar can be used to detect atmospheric phenomena. MIT researchers found that hydrometeors attenuate and scatter back radiation to the radar antenna, which allow for their detection. They proved that this could be accomplished out to ranges of 240 km at 3 and 10 cm wavelengths.

Since this discovery, radar stations have been installed worldwide in order to increase meteorological situational awareness and improve public safety. The primary weather radar in operation across the United States is the Weather Surveillance Radars-1988 Doppler (WSR-88D). Figure 2 shows the locations of the 159 WSR-88Ds installed in the United States and at DoD installations across the globe. This system of weather radars is called the Next-Generation Radar (NEXRAD) network and is a

joint effort by the Department of Commerce, Defense, and Transportation. The controlling agencies include the National Weather Service (NWS), Air Force Weather, and Federal Aviation Administration (FAA) (NWS, 2018). The WSR-88D has a maximum range of 230 km and operates at 10.5 cm wavelength. It has a peak transmission power of 700 kW, making it one of the most powerful weather radars in the world. The NEXRAD network was upgraded in the early 2010s to include DP capabilities.

2.2.1 Dual-Polarization Radar

DP radar is a type of weather radar that functions by emitting two separate electromagnetic (EM) radiation pulses in both a horizontal and vertical orientation (NWS, 2017). Traditional weather radar functions by emitting horizontal EM radiation, which allows the radar to detect only the horizontal dimension of a target. However, with DP radar the returning radiation provides both the horizontal and vertical cross-sections of targets, thus allowing meteorologists a better estimate of the shape, size, and variety of targets. Figure 3 shows the outward emittance of horizontally and vertically-imposed EM radiation on a target by a DP radar, and the advantages of using this type of radar to detect certain meteorological phenomena. Before 2011, all WSR-88Ds operated as traditional weather radars. Despite the relatively recent improvements to the NEXRAD network, DP radar technology has been studied extensively throughout the late 20th century. DP radar was invented in the 1980s by National Oceanic and Atmospheric Association (NOAA) researchers in Norman, Oklahoma (NWS, 2017). The high familiarity of the technology among forecasters allowed for rapid implementation of DP into the NEXRAD network.

Depending on the mode of operation, average WSR-88D power output ranges from 300 W to 1300 W (NWS, 2018). The two primary modes of operation for WSR-88Ds are clear air mode and precipitation mode. The radar uses clear air mode when no

8
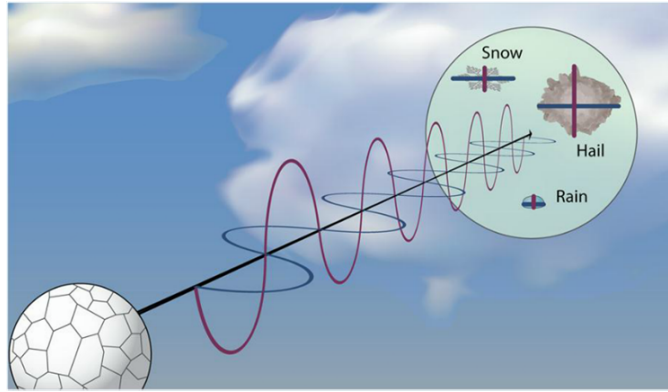
Figure 3. A schematic showing how DP radar functions. The DP technology allows for the detection of the horizontal and vertical extent of targets based on the returned frequencies of the backscatter. Adapted from NWS (2017).

precipitation is detected and undergoes 10-minute volume scans. These longer scans enable an increase in radar resolution and heightened sensitivity. Normal echoes in this mode can include insects, birds, dust, or even temperature and moisture gradients in the atmosphere. In precipitation mode, the radar completes a volume scan every 4-6 minutes, depending on the volume coverage pattern (VCP) in use. A VCP consists of multiple 360° degree radar scans of the atmosphere, which samples a set of increasing elevation angles (NWS, 2018). The three clear air mode VCPs are: 31, 32, and 35. VCP 31 and 32 contain the same elevation angles but vary in their pulse repetition frequency (PRF). PRF is the length of time between radar pulses. A lower PRF means that the signal can travel farther, while a higher PRF allows for the velocity detection of targets (NWS, 2018). The optimal balance between a low and high PRF and distance or velocity is what is known as the doppler dilemma. This occurs as a result from the radar being unable to detect a pulse because it transmitted a new pulse before detecting the original one. This problem means that there is an inverse relationship between the maximum range of a radar and its velocity (NWS, 2018). Such velocity aliasing problems are reduced by the use of certain precipitation VCPs.
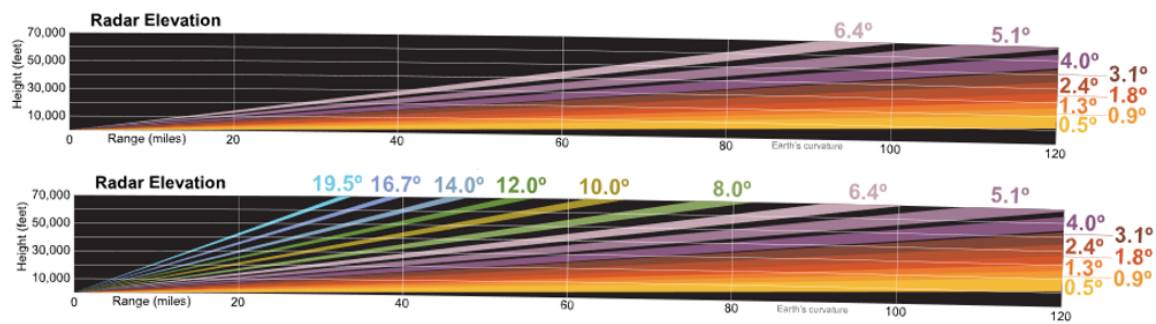
Figure 4. A schematic showing the differences in elevation angles for a clear air mode VCP (top) and a precipitation mode VCP (bottom). Adapted from NWS (2018).

Precipitation mode has four VCPs: 12, 121, 212, and 215. Figure 4 shows two example VCPs, one for clear air mode (top) and precipitation mode (bottom). Each precipitation VCP has a specific purpose and varies either by elevation angle, PRF, or scan time. For instance, in VCP 121, the radar omits higher elevation scans for an increase in radar samples across the lower levels (NWS, 2018). This is particularly useful for tropical systems, where the lower elevation scans are ideal in detecting the movement of spiraling rainbands. All radar data analyzed throughout this study was retrieved from WSR-88Ds configured in one of these four precipitation mode VCPs.

Weather radar data output from the WSR-88D is categorized either as Level II or Level III data. Level II data is the digital base that the radial base data and DP variables output from the signal processor within the radar data acquisition unit (NWS, 2018). It contains both of the base and DP radar products that will be discussed in the next section. Comparatively, Level III data is also output data from the radar product generator, however, it is instead post-processed into useful weather products used by meteorologists and forecasters to assist in weather analysis, forecasts, warnings, and weather tracking (NWS, 2018). It contains unique radar products such as the Hydrometeor Classification Algorithm, Echo Tops, and Melting Layer. The two primary Level II products used within this study are now discussed.

10

2.2.2 Reflectivity

Reflectivity, denoted as Z, is the measure of the reflectance of the horizontally-imposed EM radiation back to the radar antenna (NWS, 2018). More specifically, the reflectivity values are estimated from the received power P_R. Reflectivity is the most commonly used radar product in short-term forecasting and lightning studies because of the linear dependence of reflectivity to precipitation amounts (Travis, 2015). The returned power P_R depends on many factors including the technical characteristics of the radar, the propagation conditions, the distance to the target, and its reflectivity Z. The meteorological radar equation, as given by Meischner (2005), is as follows:

$$P_{\mathrm{R}} = \frac{\pi^3 P_{\mathrm{T}} G^2 G_{\mathrm{R}} \Theta^2 c\tau |K|^2 Z}{2^{10} \ln(2) \lambda^2 r^2 L_{\mathrm{atm}}^2 L_{\mathrm{MF}}} \tag{1}$$

where P_{T} is the peak transmitted power at the antenna, G is the total antenna gain, G_{R} is the total receiver gain, Θ is the antenna 3 decibel (dB) beam width, $|K|^2$ is the constant factor, λ is the wavelength of the transmitted EM radiation, L_{atm} is the one way atmospheric attenuation between the radar antenna and the target, and L_{MF} is the matched filter losses. This equation is valid under the assumption that the beam formed by the antenna is circularly symmetric and that the resolution volume is filled with precipitation. Using the relationship $c = \lambda f$, the constants from the power equation (1) can be rearranged into C_{R} and solved for Z to be represented as:

$$Z = C_{\mathrm{R}} \cdot r^2 \cdot L_{\mathrm{atm}}^2 \cdot P_{\mathrm{R}}. \tag{2}$$

Z has standard units of $\mathrm{mm}^6\mathrm{m}^{-3}$, where radars provide an estimate of the reflectivity value Z at range d along the beam. The returned energy can span a large range of values, which is why Z is usually expressed logarithmically as dBZ (Petty, 2006). Z can be converted from standard units dB to units dBZ using the following

11

equation from Petty (2006): $Z[\text{dBZ}] = 10\log_{10}(Z)$. An increase in reflectivity by 10 dBZ corresponds to a factor ten increase in Z expressed in standard units and an increase of 20 dBZ implies a hundred-fold increase in reflectivity. Typical Z values can vary from -20 dBZ to 70 dBZ, depending on the range of targets being sampled and the type of weather event. Equation (2) can also be expressed in terms of the Rayleigh regime and calculated using the following equation given by Petty (2006):

$$Z = \int_0^\infty n(D)D^6 dD \tag{3}$$

where n is the number of droplets and D is the diameter of the droplet size being sampled. Reflectivity is used as a basis in the creation of many DP and Level III products. The DP radar product used within this research study is next discussed.

2.2.3 Differential Reflectivity

The primary DP radar product used within this study is called differential reflectivity, henceforth referred to as Z_{DR}. It is used to calculate the ratio of backscattered horizontal and vertical reflectivity in units dB. This is useful in detecting the shape or the reflectivity-weighted axis ratio of targets within a radar volume scan (Kumjian, 2013). For perfectly spherical targets, where the horizontal and vertical polarizations are of equal power, the Z_{DR} is equal to 0 dB. For Rayleigh scatterers, where the particles are smaller compared to the radar wavelength, particles aligned in the horizontal plane produce positive Z_{DR} and those aligned in the vertical direction produce negative Z_{DR} (Kumjian, 2013). Z_{DR} is also affected by the physical composition and density of particles, which can enhance the Z_{DR} by an increase in the complex refractive index. For instance, water droplets have a higher Z_{DR} than an ice pellet of the same size and shape due to the greater complex refractive index of water (Kumjian,

12

2013). This phenomenon can skew interpretation of this radar product if it is not used correctly. Z_{DR} is calculated using the following equation from Meischner (2005):

$$Z_{DR} = 10 \log \frac{z_H}{z_V} \tag{4}$$

where z_H is the horizontal reflectivity factor, and z_V is the vertical reflectivity factor. If reflectivity is measured logarithmically, equation (4) can be simplified to:

$$Z_{DR} = Z_H - Z_V. \tag{5}$$

Z_{DR} varies greatly for different hydrometeors. Figure 5 displays the typical values of Z_{DR} across different meteorological and non-meteorological targets. In rain, Z_{DR} tends to be positive with increasing drop size. This is caused by the aerodynamic drag induced onto a falling drop. The drag forces cause larger rain drops to become oblate in shape, while smaller drops remain spherical due to their smaller surface area. The flatter shape of the drop causes an increase in Z_H, which results in a positive Z_{DR}. Hail and graupel Z_{DR} signatures are more complex than rain drops. This is due to Z_{DR} changing as a function of hail and graupel size, shape, and liquid water content (Kumjian, 2013). Increasing positive Z_{DR} values of hail and graupel particles are indicative of wetter and/or melting conditions. A Z_{DR} of zero can result from tumbling hail, due to the appearance of a spherical target by the radar antenna. Negative Z_{DR} values, though rare, are the result from the complicated effects of resonance scattering on large Mie scatterers, such as hail ≥ 5 cm (Kumjian, 2013).

As with all radar products, Z_{DR} is most useful when it is utilized in combination with additional traditional and DP radar data. This process provides a system of checks and balances that is used to confirm or deny the presence of particular weather phenomena. For instance, in order to verify the existence of hail and graupel within

13
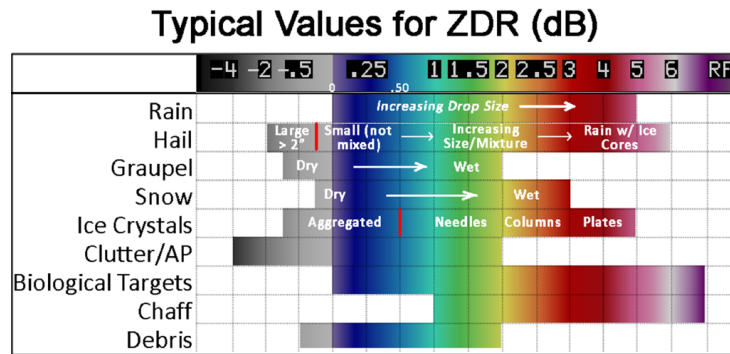
Figure 5. A graphic displaying the range of Z_{DR} values attributed to typical meteorological and nonmeteorological targets. Adapted from NWS (2018).

a towering cumulonimbus, Z_{DR} is often used with Z. An area of increased Z overlaid onto a region of positive Z_{DR} can indicate the presence of hail and/or graupel and suggest that the cloud is undergoing electrification processes. This analysis process can prompt meteorologists of an impending lightning strike and ultimately allow for the timely issuance of the necessary warnings needed to increase public safety.

2.3 Lightning Detection

This section describes the primary means of detecting lightning strikes for use within this study. It also details how the chosen lightning detection network operates, common errors associated with it, its origins, and its advantages over other sensors.

The widespread dangers lightning poses on space launch missions and the public is mitigated by numerous lightning detection networks installed across the nation. The primary suite of detection sensors installed in the United States is called the National Lightning Detection Network (NLDN) and is commercially operated by Vaisala^{TM}. Since installation in 1989, total lightning flash detection efficiencies have ranged between 50-60% (Vaisala, 2018b). These lightning detection rates, though acceptable for general forecasting purposes, are too low for USAF space launch efforts.

CCAFS/KSC boasts a dense network of lightning detection instruments. In fact, it is one of the most sophisticated areas in the world in terms of meteorological instruments due to the fragile nature of space vehicles (Roeder, 2018). The first system used by the 45 WS for total lightning detection was called the Four-Dimensional Lightning Surveillance System (4DLSS). The 4DLSS was a suite of lightning detection instruments unique to CCAFS/KSC which demonstrated a flash detection rate of 100% (Roeder, 2010). The 4DLSS detected lightning using two pre-existing systems: the Lightning Detection And Ranging System (LDAR) for IC/CC/CA lightning and the Cloud-to-Ground Lightning Surveillance System (CGLSS) for CG lightning. A portable version of the LDAR, that has higher flash detection rates than the NLDN and used primarily within this study, is called the Lightning Mapping Array (LMA).

2.3.1 Lightning Mapping Array

Invented by researchers in 1998 at NMT, the LMA is a portable, 3-D total lightning detection network. The LMA consists of 9 to 13 instruments spread around an area of up to 80 km in diameter (Krehbiel et al., 2001). It operates by detecting sources of EM radiation produced by lightning step leaders during dielectric breakdown and measuring their time-of-arrival (TOA) to the individual sensors. The EM radiation measured are radio frequencies in an unused very high frequency (VHF) band (60-66 MHz) (Thomas et al., 2004). The LMA network is patterned after the LDAR system developed at CCAFS/KSC by Carl Lennon in the 1990s (New Mexico Tech, 2018).

The use of TOA measurements for lightning detection was pioneered by David Proctor. In Proctor (1981), the author used ground-based VHF receivers to trace the paths of outgoing EM radiation following lightning flashes. Proctor found that lightning channels could be mapped in 3-D space and time based on their arrival at each of the receivers. In modern TOA-based detection sensors, hyperbolic surfaces are
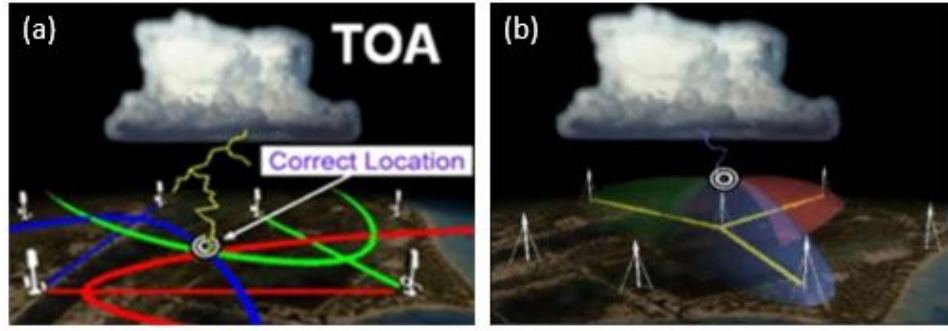
Figure 6. (a) 2-D intersection of hyperbolae indicating the return stroke location via TOA differences; (b) 3-D intersection of hyperbolae pinpointing the step leader location via TOA differences. Adapted from Roeder (2010).

used to identify the locations of lightning strikes. This is accomplished by detecting TOA differences of the VHF pulses in sensor pairs. When a pair of sensors detects a pulse, a hyperbolic volume can be created. The stepped leader is located by the intersection of four hyperbolae. Figure 6 displays both a 2-D and 3-D representation of intersecting hyperbolae using the TOA-differencing technique. The best location of the stepped leader is solved via statistical Chi-Squared minimization (Roeder, 2010).

A minimum of six stations is required to build a solution, in order to solve for the four unknowns: x, y, z, and t (Thomas et al., 2004). NMT LMAs use the following equation for TOA calculations in order to determine the position and time of a radiation source:

$$t_i = t + \frac{\sqrt{(x - x_i)^2 + (y - y_i)^2 + (z - z_i)^2}}{c} \tag{6}$$

where t_i is the time of arrival of the radiation on station i, t is the time of radiation occurrence by the lightning, x, y, z is the location of the radiation in Cartesian coordinates, x_i, y_i, z_i the location of the radiation on station i in Cartesian coordinates, and c the speed of light (New Mexico Tech, 2018). Using this calculation method, the LMA can locate hundreds to thousands of radiation sources per lightning flash. The

16

two additional sensors in the LMA network are necessary in order to filter local noise events. Local noise events are produced by the electrical discharge of power components causing ionization effects onto the air. This phenomenon is known as corona discharge and can occur from a variety of natural and man-made sources. The main cause of noise events in LMA networks are a result from nearby electric transformers and power lines (Thomas et al., 2004). Corona discharge can also occur in storm conditions when elevated objects are exposed to strong electric fields. In addition to providing a means to filter noise, the two redundant sensors also add statistical degrees of freedom.

There are numerous advantages in using the LMA for lightning-related research over traditional lightning detection networks, as summarized by The University of Oklahoma (2005). First, VHF source densities are updated every 2 min, as opposed to the 5 min volume scans of radars. This allows for more up-to-date lightning information to be used operationally in forecasts. Second, because IC/CC lightning precedes CG lightning by an average of 5 to 10 min, an LMA is able to detect the first occurrence of lightning. This can cue forecasters to strengthening thunderstorms and allows for total lightning detection. Third, cloud lightning flash rates are correlated with thunderstorm initiation, development, and dissipation. By utilizing the ability of LMAs to detect lightning flash rates, forecasters can more accurately analyze thunderstorms and use them to improve forecasts. This is compared to traditional lightning detectors that only detect CG or IC strikes. Lastly, VHF sources enable better approximations of storm echo top heights. Echo Top heights is a Level II radar product that depicts the highest detections of precipitation (defined as a region of $Z \geq 18.5$ dBZ) by the WSR-88D. Echo Tops can be used to assess the strength of a thunderstorm. Many lightning forecast methods make use of this radar product because of the correlation of Echo Tops to updraft strength (Yang and King, 2010).

17

2.4 Previous Research

This section highlights previous research studies concerning weather radar and lightning initiation. It focuses primarily on the two lightning prediction methods from Gremillion and Orville (1999) and Travis (2015). Findings of a similar study (Olsen, 2018) regarding the application of Travis' DP radar parameters to the Washington, D.C. area are also discussed.

2.4.1 Reflectivity and Lightning

The relevance of Z parameters to lightning onset has been studied extensively since the invention of the WSR-88D. Studies have been conducted across different geographic regions in order to characterize specific lightning initiation signatures on weather radar. Generally, most radar/lightning studies dictate that an average of 35 dBZ at the $-10°$C height is best at predicting lightning onset (Yang and King, 2010).

The primary Z and lightning initiation study utilized in this research study is one developed for the CCAFS/KSC area in Gremillion and Orville (1999). Henceforth referred to as the Gremillion Method, this study analyzed 39 airmass thunderstorms against NLDN and non-DP radar data with the goal of finding the best predictor of CG lightning. They accomplished this by first defining a Lightning Initiation Signature (LIST) as the value of maximum Z that is sustained for at least two consecutive volume scans. Each thunderstorm was analyzed at the $-10°$C, $-15°$C, and $-20°$C thermal levels at different Z thresholds. For their cases, Gremillion and Orville found that the highest performing LIST in terms of highest detection rates and minimal false alarms was 40 dBZ at the $-10°$C thermal height. This produced a detection rate of 84% with a false alarm rate of 7%. These findings were a significant reduction from the previous CCAFS/KSC rule of thumb for lightning nowcasting of 45 dBZ at the $-10°$C level. Gremillion and Orville noted that this lightning forecast method

18

had the potential for use in similar geographical regions across the Southeast United States, where airmass thunderstorms develop from identical sources.

2.4.2 Dual-Polarization Parameters and Lightning

With the implementation of DP radar into the NEXRAD network in the early 2010s, research studies pertaining to DP radar parameters and lightning onset emerged. The main DP parameters tested in this study are from Travis (2015), where the author optimized 249 airmass thunderstorms at CCAFS/KSC with the goal of improving total lightning forecasts. Using a similar methodology as Gremillion and Orville (1999), Travis tested each storm at the $-5°C$, $-10°C$, $-15°C$, and $-20°C$ thermal heights against the 4DLSS, using a variety of different Z and DP parameters.

Travis used hits, misses, false alarms (FAs), and correct rejections (CRs) to record how well his method performed. A hit was recorded if the predictor threshold was met or exceeded prior to a lightning strike and the cell produced lightning. Misses, however, were noted if lightning occurred but without satisfying the necessary thresholds. An FA was recorded if the radar parameters were met or exceeded, but lightning did not occur. A CR was used if the parameters were not met and the cell did not produce lightning. Travis then used scatter plots to compare both lightning-producing and non-lightning producing cells against DP variables at each thermal height using different Z values. Using additional statistical methods, the author optimized each Z and DP variable combination across all lightning-producing cells. Travis found that the best performing set of Z and DP parameters to be $Z \geq 36.5$ dBZ with $Z_{DR} \geq 0.31$ dB at the $-10°C$ thermal height. This combination of radar parameters maximized detection rates and lead times, while simultaneously minimizing FAs. Travis recommended testing the prediction method in different areas with similar total lightning detection networks in order to quantify its use in other area of responsibilities (AOR).

19
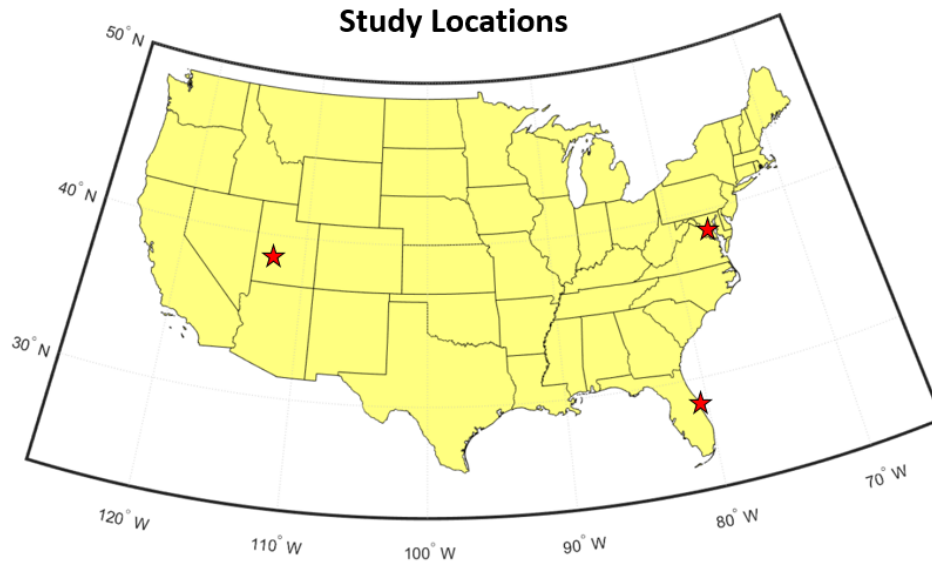
Figure 7. A map showing the research study locations of Gremillion and Orville (1999); Travis (2015) (Florida), Olsen (2018) (Washington D.C.), and this research study (Utah). It is interesting to note that the latitude of Olsen (2018) and this study is identical at 39°N. Graphic produced using MATLAB.

Olsen (2018) was the first attempt at testing Travis' DP parameters in a new region. Olsen tested the CCAFS/KSC radar parameters in Washington, D.C. Figure 7 shows the research locations of Gremillion and Orville (1999), Travis (2015), Olsen (2018), and this study. Olsen concluded that Travis' method did not perform well in Washington, D.C. Expanding the research efforts of Olsen by testing both the Travis and Gremillion method in a new environment is the next logical step in order to continue radar and lightning research, as tests in a new area can infer new knowledge about DP and non-DP radar data. Utah serves as the ideal test area due to significant climate, terrain, and elevation differences from CCAFS/KSC and Washington, D.C. Also, the presence of a pre-existing lightning detection network similar to the one used in Travis (2015) and Olsen (2018), multiple WSR-88Ds, and the high number of airmass thunderstorms that form there make Utah the optimal study location.

III. Methodology

3.1 Sources of Meteorological Data

This section details the sources of lightning, radar, and upper air data utilized within this study. Specifically, the location of the LMA, WSR-88Ds, rawinsonde sites, the data retrieval process, and data configuration.

3.1.1 Lightning Data

Archived Utah LMA data was downloaded from the NMT Utah Lightning web page (New Mexico Tech, 2018). LMA data was generously provided from Dr. William Rison, Professor of Electrical Engineering at NMT and one of the main inventors of the LMA. The Utah LMA is also known as the Telescope Array (TA) LMA, due to its proximity to the National Science Foundation's Telescope Array Project, and will henceforth be referred to as such. Figure 8 shows the TA LMA network, spread around a dry lake bed in southwestern Utah. The archived LMA files were broken down by folder into 10 min increments, totaling 144 total separate files for one day. Next, files were downloaded according to the day and time of interest. A time period of 10 min was downloaded before cell formation, as indicated on radar, to ensure complete storm coverage. Each data file contained thousands of lines of text denoting lightning strike information and station health. Detected strikes were organized as: time in Universal Time Coordinated (UTC) seconds, latitude/longitude, and altitude.

There were a few time periods of missing data, but overall the data gaps had little impact on the outcome of the research. The most significant data outage occurred from January 2014 to July 2015, when a hard drive containing the LMA data was inadvertently deleted (Rison, 2018). This restricted the dataset to only three and a half years of data, instead of five years which could have potentially added several

21

Figure 8. A map showing location of the TA LMA within the state of Utah. The black stars represent the individual LMA sensors. Graphic created using MATLAB.

more cases to this study. Data collection was limited to only warm-season months, May through September, from August 2015 to August 2018. This was accomplished in order to remain consistent with previous research studies and to construct a complete three-year climatology of Utah thunderstorm occurrence.

3.1.2 Radar Data

The two WSR-88Ds utilized were Cedar City, Utah (KICX) and Salt Lake City, Utah (KMTX). Figure 9 shows the location of KICX and KMTX relative to the TA

LMA. KICX is located approximately 145 km southeast of the TA LMA center and is at 10,754 ft MSL (NWS, 2018). The placement of the radar at such a high elevation is to ensure that detection is optimized and not obstructed by nearby mountains. KMTX, however, is located 250 km northeast of the TA LMA center and is positioned at 6,592 ft MSL (NWS, 2018). Similar to KICX, KMTX is placed high enough to ensure no interference from the mountainous terrain. KICX was used as the primary radar in this study, because of its closer distance to the center of the LMA network than KMTX. However, for cells that formed north of the LMA, KMTX was utilized to interrogate storms because of its better coverage of that area over KICX. This convective cell selection process will be discussed in greater detail in Section 3.2.

Archived Level II NEXRAD weather radar data was downloaded from the National Centers for Environmental Information (NCEI) web page at NOAA (2018b). The radar archives were comprised of compressed files that contained data for each complete radar scan, which varied in size dependent on the VCP in use. File sizes varied greatly depending the on the severity of the weather. For instance, on active thunderstorm days where there were numerous convective cells or a passing cold front, radar files could be as large as 15 megabytes. Quieter and less active days, however, with little-to-no thunderstorm activity produced file sizes averaging 500 kilobytes.

3.1.3 Miscellaneous Data

In addition to lightning and radar data, archived sounding data was analyzed to identify the $-10°C$ thermal height. For the state of Utah, the only rawinsonde data originates from Salt Lake City which is 200 km away from the center of the TA LMA. Using this upper air data for the testing area was problematic because it is too far away to assume an identical atmosphere. This was confirmed by comparing actual rawinsonde data against model data in the testing area. In order to remedy the lack of
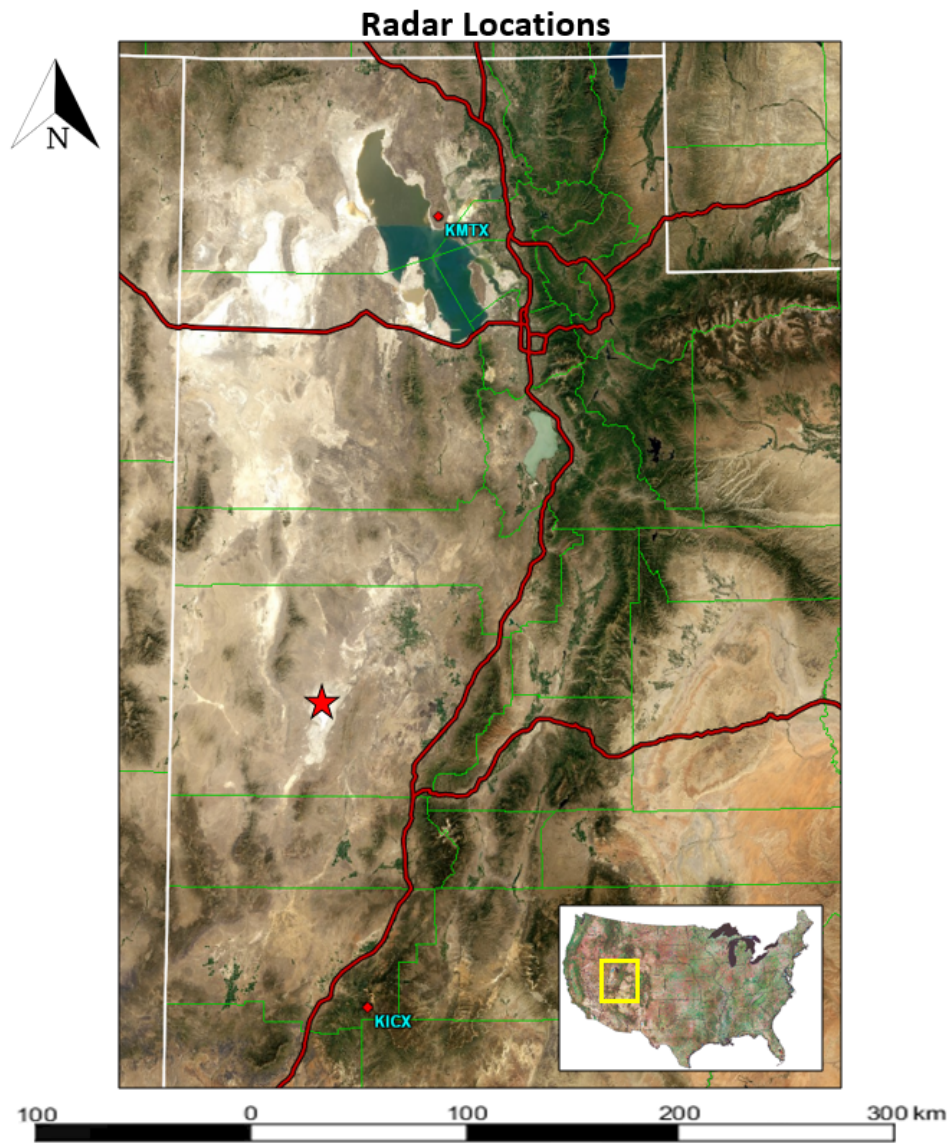
Figure 9. The locations of the two weather radars, KICX and KMTX, are marked by the red diamonds. The red star between the two radars represents the center of the TA LMA. Graphic created using MATLAB.

sounding data in southwest Utah, two additional surrounding rawinsonde sites were considered: Grand Junction, Colorado and Las Vegas, Nevada. Figure 10 depicts the locations of the three sounding locations in relation to the center of the TA LMA. All three sounding locations create an isosceles triangle that encompasses the TA LMA. The centroid of the triangle was calculated and found to be 75 km southeast of the TA LMA center. Employing a spatial averaging technique of the locations provided a better estimate of the $-10°C$ thermal height than using Salt Lake City's data alone.

The upper air data was downloaded through a support request submitted to the Air Force's Combat Climate Center, the 14 WS. All dates between 1 May 2015 and 31 August 2018 were downloaded. The 0 UTC and 12 UTC soundings for all three sites were averaged to calculate a new total daily $-10°C$ average. This total daily average was used as the $-10°C$ thermal height across the testing area. This calculation was repeated for each case in the dataset to ensure accurate heights throughout this study.

3.2 Convective Cell Selection

In order to ensure a fair comparison of this study to Olsen (2018), the methodology applied to this experiment needed to be as similar as possible to Olsen. This helps to eliminate bias and minimize error which can lead to inaccurate findings and results.

The initial dataset was gathered using the NOAA NCEI Interactive Radar Map Tool (NOAA, 2018a) to locate isolated thunderstorms. This tool functions by creating a reflectivity mosaic of the NEXRAD network, thus allowing the user to observe nationwide thunderstorms using one tool. Range rings were then established around the TA LMA and both radars. A radius of 100 km was chosen for the TA LMA because flash detection efficiency exceeds 95% in this range and source detection efficiency exceeds 70% (Olsen, 2018). This is also the same range used around the 4DLSS in Travis (2015) and the NLDN in Gremillion and Orville (1999). Around

25
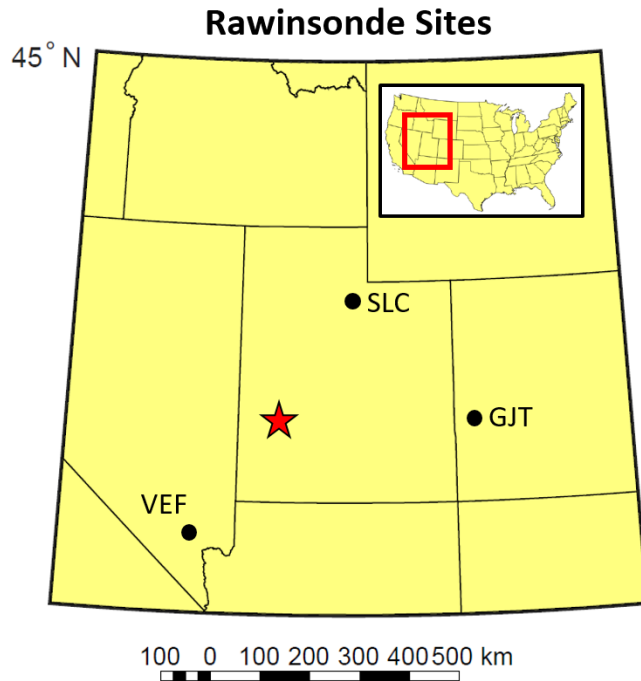
Figure 10. The black dots indicate the rawinsonde locations: Las Vegas, Grand Junction, and Salt Lake City. The red star is the center of the TA LMA network. Each sounding location is approximately of equal distance from the center of the TA LMA. Graphic created using MATLAB.

the two radars, 160 km radius rings were established. This number was found to be the optimal detection range based on radar coverage maps in NOAA (2018a). Large terrain features in Utah caused radar coverage to be sparse and became a significant factor when narrowing down the dataset. The radar range used in this study differs from the 85 km radius used in Olsen (2018) and the radar ranges from Travis (2015) and Gremillion and Orville (1999). This was caused by the radar coverage in southwest Utah which is less dense than around Washington, D.C and CCAFS/KSC. Additionally, Washington, D.C and CCAFS/KSC do not have mountainous terrain like Utah. Thus, it was imperative for the continuation of the research to extend the radar ranges past previous studies' ranges to compensate for the poor radar coverage. Figure 11 shows the range rings established around the TA LMA, both radars, and

www.manaraa.com
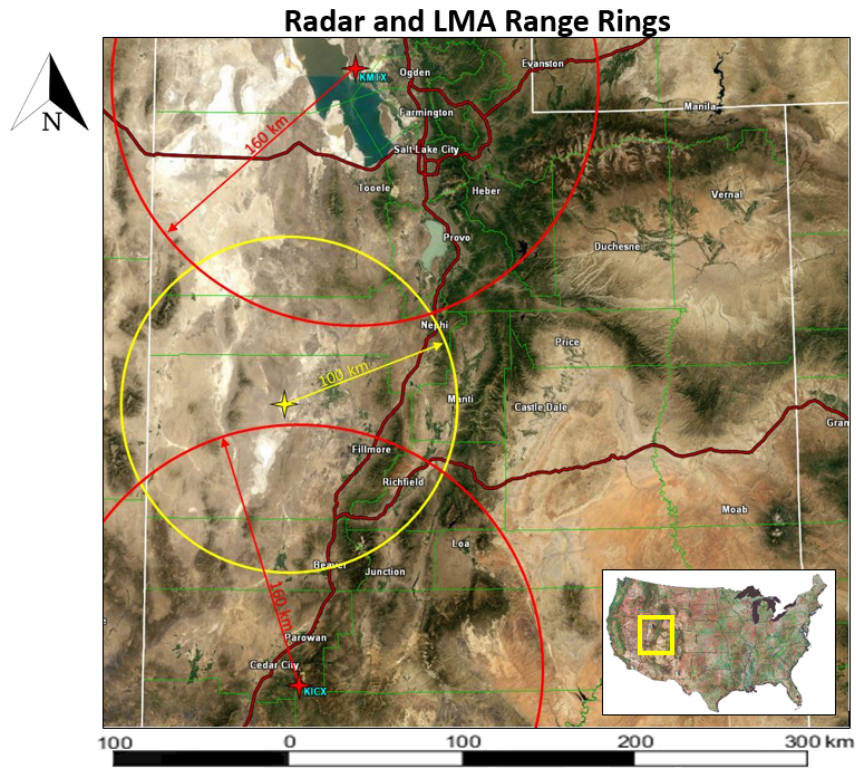
Figure 11. Range rings representing the bounds for the northern and southern testing areas. The yellow star is the center of the TA LMA and the red stars are both radars. Only cells that formed within the overlapping LMA/radar rings were considered for the final dataset. Graphic created using MATLAB.

the northern/southern testing areas. A cell needed to form within either one of the two overlapping LMA and radar rings in order to be considered for the initial dataset. After a cell was found that formed in either testing area, its formation and dissipation time was recorded into a spreadsheet, along with its location in latitude and latitude coordinates. This process was repeated for each day containing isolated cells in the northern/southern testing areas, increasing the initial dataset well over 300 cases.

Once all of the radar data was downloaded, it was viewed within Gibson Ridge 2 Analyst™ (GR2Analyst) software. GR2Analyst is an advanced NEXRAD Level II analysis application, which allows for the interrogation of traditional and DP radar data at high resolution (Gibson Ridge Software, 2018). GR2Analyst can create cross-

27

sections and 3-D volumetric renderings, which allow for the examination of radar output at altitude. The cross-section tool was the primary instrument used within this study because it allowed the researcher to quickly analyze the vertical extent of thunderstorms and observe whether or not they met testing threshold requirements. The position and swing functions within this tool were used to adjust the slice, ensuring thorough examination of each cell. The GR2Analyst volumetric instrument was also used in addition to the cross-section tool to construct a 3-D representation of Z. The isosurface function was employed, which enabled the user to set the 3-D basis at any Z value. For instance, setting the isosurface basis to the 36.5 dBZ threshold from Travis (2015), presented the user with a 3-D rendering of the vertical construction of a cell at this particular Z value. This allowed for a straightforward method of testing varying Z parameters. Figure 12 shows GR2Analyst output of Z during an airmass thunderstorm using (a) the volumetric instrument and (b) the cross-section tool.

After all of the radar files were downloaded, they were ingested into GR2Analyst for viewing. The initial 300 convective cell dataset was narrowed down to the final dataset by applying strict elimination criteria. Similar to previous lightning-related studies accomplished by Thurmond (2014), Travis (2015), and Olsen (2018), the Larsen area method was used to determine if a cell was a suitable candidate. The Larsen area method was initially developed in order to locate lightning with radar Z patterns at significant thermal levels (Larsen and Stansbury, 1974). The cells in this study were analyzed for a Larsen area defined by a horizontal Z threshold of ≥ 30 dBZ at the $-10°$C thermal height. This thermal height is significant to thunderstorm charge structure in terms of indicating the lower bounds of the main charging region (Olsen, 2018). The cells were then viewed and tested within GR2Analyst to ensure they met the isolated criteria. This was completed using the isolated convective cell criteria from Patton (2017), where a cell was considered isolated if it had no storms

28
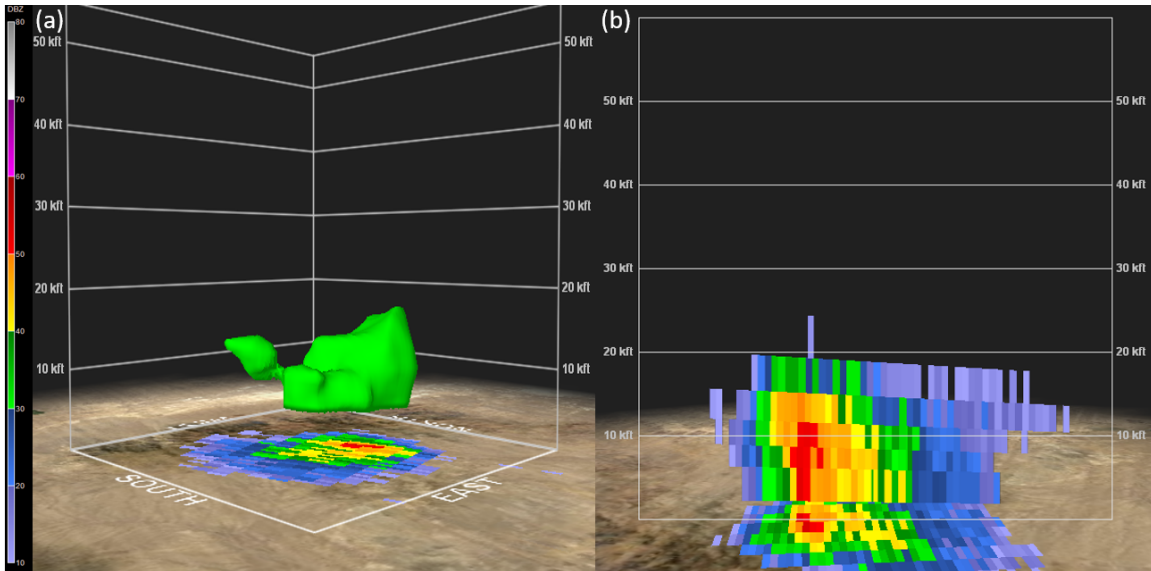
Figure 12. Reflectivity images showing the volumetric instrument (a) with an isosurface basis set to 36.5 dBZ and the cross-section tool (b) showing the vertical extent of the same cell. Images produced using GR2Analyst.

with connecting Z values of ≥ 15 dBZ. This isolated criteria reduced the dataset by 75 cases. Radar coverage was next investigated to ensure adequate storm coverage.

The isolated convective cells were then analyzed to determine if the volume scan elevation angles of both radars intersected a cell of interest at the $-10°$C thermal height. This was accomplished by creating cross-sections of cells and observing whether or not the $-10°$C height was detected by the radar. GR2Analyst cross-sections display the altitude in terms of height above the beam. One cannot assume the heights on a GR2Analyst cross-section as MSL heights, because of the significant terrain and elevation differences in Utah compared to Washington, D.C. and Florida. To correct for this, the radar elevation had to be subtracted by the total daily average $-10°$C height and the elevation of each respective testing area had to be added. To illustrate this, take the following example for a case on 1 May 2018 near the KICX radar, where the average $-10°$C height was 13,253 ft. The elevation of the KICX radar (10,754 ft) was first subtracted from the $-10°$C height, then the average elevation of the south-

29

ern testing area was added (4,750 ft). The resultant number of 7,249 ft provided the altitude of the $-10°C$ height, as indicated on a GR2Analyst cross-section using KICX radar. Completing this procedure for KMTX was identical to KICX, except for the differences in elevations for the northern testing site (5,500 ft) and KMTX (6,592 ft). Radar coverage issues eliminated approximately 100 cases from the initial dataset.

After verifying that the initial dataset had adequate radar coverage, the raw LMA data was examined to determine station health. As previously mentioned, a healthy station consisted of six or more active sensors in the network, as six sensors were used to build a solution. Cells that had any indications of less than six active stations in the LMA files were discarded from the initial dataset. This procedure was repeated for the WSR-88Ds to verify that the radar data was reliable. Using the NOAA (2018b) web page, days containing the initial dataset were examined to determine whether or not the radar was fully operational. A visual status display was created for each day indicating radar status by color. If a radar was in 'Maintenance Mode' or 'Unknown Mode', the radar data was considered unreliable and promptly eliminated from the dataset. Figure 13 shows the status graph of KICX radar on 1 May 2018. This quality check of both LMA and radar data reduced the initial dataset by 25 cases.

After all elimination requirements were applied, the initial dataset was reduced to a final dataset of 102 cases. The final dataset contained the cells used in the testing of both Travis' and Gremillion's lightning prediction methods. All of the information pertaining to cell formation and dissipation time, location, and $-10°C$ heights were recorded into a spreadsheet. Figure 14 displays Utah thunderstorm climatology against the hourly and monthly breakdown of cells in the final dataset. The thunderstorm climatology histogram was produced using state-wide Operational Climatic Data Summary (OCDS) data obtained from the 14 WS. Similar to Travis (2015) and Olsen (2018), most thunderstorms within the final dataset formed in the
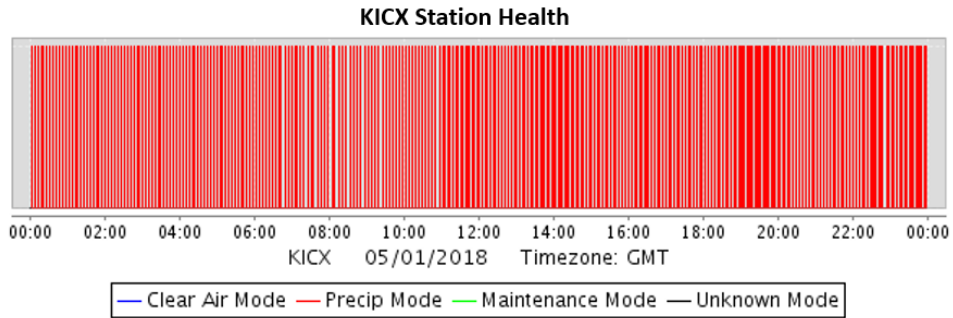
Figure 13. An example radar status graph indicating KICX station health for 1 May 2018. If the radar was in Maintenance Mode or Unknown Mode, the case was removed from the initial dataset over data quality concerns. Adapted from NOAA (2018a).
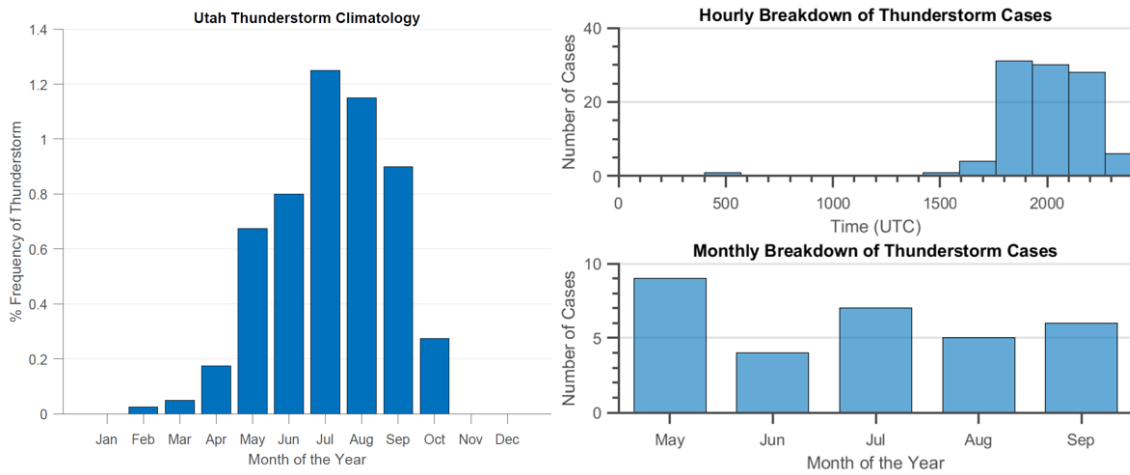
Figure 14. Histograms displaying Utah thunderstorm climatology by frequency and the hourly and monthly distribution of thunderstorm cases in the final dataset. A peak in thunderstorm formation is observed in the latter half of the day, while May and July see the highest number of cases. Climatology data courtesy of the 14 WS. Histograms created using MATLAB.

31

latter half of the day. However, the spread of cases was different from both studies. Travis and Olsen both saw a Gaussian distribution with a peak in July and a minimum in May/September. Utah's case load had a more even spread throughout the year, with May/September having the highest number and June/August the lowest.

3.3 Lightning Initiation Criteria Testing

After the final dataset was firmly established, the lightning prediction methods from Travis (2015) and Gremillion and Orville (1999) were tested. In order to apply these thresholds, the LMA files first needed to be examined to determine whether or not lightning occurred in the area of cell formation. This was accomplished using MATLAB code, with the use of 'for loops' to determine when and where a lightning strike occurred. Using the previously recorded latitude and longitude coordinates of the cells, the locations were ingested into MATLAB and ran against the LMA files in nested loops. If lightning occurred, the MATLAB code stopped and displayed a time of lightning initiation in UTC seconds. Another string of code was then used to convert the UTC seconds to a more readable 'HH:mm:ss' format. This was the time recorded into the spreadsheet. If no lightning occurred, MATLAB revealed that 'Lightning Does Not Exist' (DNE) and was recorded as such. Each case was manually verified against a visual display of the TA LMA showing lightning locations and GR2Analyst to ensure that the lightning was associated with the specified case rather than another passing storm. This was also the method used to eliminate noisy/erroneous LMA sources.

Once the MATLAB code was ran for each case and the times were recorded in the spreadsheet, GR2Analyst was utilized to apply both Travis' and Gremillion's highest-performing radar thresholds. For Travis, the time $Z \geq 36.5$ dBZ at the $-10°$C height was met was recorded for each case, followed by the time of $Z_{DR} \geq 0.31$ dB. Similar to the system used in Travis (2015), if both thresholds were met prior to the lightning

occurrence time from MATLAB, the case was labeled as a hit. If one or both radar parameters were never met and lightning still occurred, it was recorded as a miss. An FA was recorded when no lightning occurred, but both parameters indicated otherwise. CRs were also noted when no lightning occurred and both thresholds concurred. Table 1 displays the possible forecast outcomes, based on forecast and observed criteria. If lightning occurred, the only possible outcomes were hit or miss; conversely, non-lightning cases yielded either an FA or CR. A hit indicated that the forecast method was performing well. A CR equally signaled that the selected forecast method was functioning adequately. On the contrary, misses and FAs implied that the predictor method was performing poorly. If a hit was recorded, the lead time was calculated by subtracting the difference between the time of lightning initiation (as displayed by MATLAB) and the time when both Z and Z_{DR} thresholds were met.

After Travis' thresholds were tested, Gremillion and Orville's parameters were applied to the Utah final dataset. This was accomplished using their highest preforming LIST, $Z \geq 40$ dBZ for two consecutive volume scans, at the $-10°C$ thermal height (Gremillion and Orville, 1999). Similar to Travis (2015), a hit was recorded if the Z threshold preceded lightning initiation and a miss if it occurred after. A CR was used when no lightning occurred and the thresholds were never met, and an FA recorded if the thresholds indicated lightning but none actually occurred. Forecast metrics were next calculated for both prediction methods to compare and contrast performance.

Event	Event Observed	
Forecast	Yes	No
Yes	Hit	False Alarm (FA)
No	Miss	Correct Rejection (CR)

Table 1. The list of possible forecast outcomes, given the occurrence or non-occurrence of a weather event. Adapted from Joliffe and Stephenson (2003); Travis (2015).

3.4 Forecast Metrics

The forecast outcomes and lead times computed from before were next inputted into forecast metrics. Forecast metrics are verification statistics used to evaluate the skill of a forecast. In this study, forecast metrics were used to score both lightning prediction methods. The Probability of Detection (POD) was the first metric calculated. Also known as the hit rate, it provides the proportion of lightning occurrences that were correctly forecasted (Joliffe and Stephenson, 2003), and is given as:

$$\text{POD} = \frac{\text{Hit}}{\text{Hit} + \text{Miss}}. \tag{7}$$

A POD of 1.0 is desired as it indicates a forecasting method is limiting the number of misses. However, because it does not take FAs into account, POD is not reliable in measuring the overall forecast skill. Only two of the forecast metrics rely on the number of FAs, they are the False Alarm Ratio (FAR) and Probability of False Alarm (PFA). FAR provides the probability of FA when an occurrence is forecast (Joliffe and Stephenson, 2003) and is defined as:

$$\text{FAR} = \frac{\text{FA}}{\text{FA} + \text{Hit}}. \tag{8}$$

A FAR of 0.0 is considered optimal because it limits the number of FAs in the forecast. However, like POD, FAR is not the ideal forecast metric when used alone because it is dependent on the number of hits (Joliffe and Stephenson, 2003). This ushers the need for PFA, which compares the number of FAs to CRs. It is given by:

$$\text{PFA} = \frac{\text{FA}}{\text{FA} + \text{CR}}. \tag{9}$$

34

A PFA of 0.0 is desired, but similar to FAR, this forecast metric is somewhat limited. This is because PFA is dependent on the number of FAs and CRs, which can limit forecast reliability (Travis, 2015). The Critical Success Index (CSI) is a verification statistic that provides the probability of a hit occurring no matter the forecast outcome. It assumes that the times when an event was neither expected nor observed are of no consequence (NWS, 2018). It is given as:

$$\text{CSI} = \frac{\text{Hit}}{\text{Hit} + \text{FA} + \text{Miss}}. \tag{10}$$

A CSI of 1.0 is considered a perfect score and scores near 0.0 indicate no skill (Joliffe and Stephenson, 2003). Although sometimes difficult to interpret, CSI provides additional insight into the overall performance of each lightning predictor method by rating a method's success at forecasting a rare critical event (Roeder, 2018). It was initially developed by the NWS in order to score the skill of tornado forecasts.

True Skill Statistic (TSS) is used to determine how well a method preforms at predicting the occurrence or non-occurrence of an event. It takes into account all of the outcomes from Table 1 and ranges from -1.0 to $+1.0$. A TSS of $+1.0$ is considered perfect for predicting the occurrence of an event. A TSS of -1.0 indicates the case was a perfect predictor for determining the non-occurrence of an event (Joliffe and Stephenson, 2003). A TSS score of 0.0 indicates no forecast skill. It is defined as:

$$\text{TSS} = \frac{(\text{Hit} * \text{CR}) - (\text{FA} * \text{Miss})}{(\text{Hit} + \text{Miss})(\text{FA} + \text{CR})}. \tag{11}$$

The last forecast metric used in this study is the Operational Utility Index (OUI). Developed by the 45 WS for their operations, it is optimized to test the operational utility of different lightning prediction algorithms (Travis, 2015). OUI is a non-standard performance metric that takes combines POD, TSS, PFA, and average lead

35

time into a weighting scheme that reflects the operational priorities of the 45 WS. An OUI score of 1.0 denotes optimal performance, while a score of 0.0 indicates no skill. The POD is given a weight of three because of the high emphasis placed on personnel safety. TSS is weighted at two, because it is accepted as a reliable measure of skill. Lead time is also weighted at a two in the overall calculation. PFA is weighted the least, because some FAs are accepted by the 45 WS in order to maintain a high POD. Similar to the metric used by Travis (2015), the average lead time for OUI is measured against the 45 WS standard desired lead time of 30 min and is defined as:

$$\text{OUI} = \frac{(3 * \text{POD}) + (2 * \text{TSS}) + (2 * \frac{\text{LeadTime}}{30}) + (1 * (1 - \text{PFA}))}{8}. \qquad (12)$$

As an additional measure of forecast skill in this study, two modified versions of OUI were utilized in order to better normalize the lead time term. The first is defined as OUI* and is identical to the forecast metric introduced in Olsen (2018). OUI* differs from OUI in that the 30 min lead time term is replaced in the denominator with the maximum lead time found in the analysis. OUI* is scored the same as OUI, where a score of 1.0 is perfect and a score of 0.0 is worthless. OUI* is given by:

$$\text{OUI*} = \frac{(3 * \text{POD}) + (2 * \text{TSS}) + (2 * \frac{\text{LeadTime}}{\text{MaxLeadTime}}) + (1 * (1 - \text{PFA}))}{8}. \qquad (13)$$

A recent report (Nava, 2018) studied the differences between the OUI from Travis (2015) and the OUI* from Olsen (2018). In Nava (2018), the author recalculated Travis' forecast metrics using his original hit, miss, FA, and CR count. Inputting the maximum lead time from Travis (2015) into the new OUI* calculation, Nava found that the mean/median value decreased by 0.04. The smaller mean/median value was a result from using the maximum lead time in the lead time term in the denominator. In order to determine if the 0.04 difference was significant, a statistical resampling

36

technique was utilized that suggested the two OUIs were similar. Nava concluded that the impact of the OUI equation differences between the two studies was negligible.

The third and final modified OUI is OUI†. OUI† is made to further normalize the lead time term. This forecast metric is unique to this study. Normalizing is accomplished by limiting the 'MaxLeadTime' term to 30 min (Roeder, 2018). Comparing OUI† against the previous two OUIs will indicate its usability for 45 WS operations. OUI† is scored the same as the previous two OUIs and is defined as:

$$\text{OUI}^\dagger = \frac{(3 * \text{POD}) + (2 * \text{TSS}) + (2 * \frac{\text{LeadTime}}{\text{MaxLeadTime[30]}}) + (1 * (1 - \text{PFA}))}{8}. \qquad (14)$$

3.4 Bootstrap Resampling Method

Bootstrapping is a statistical resampling technique used to estimate statistics on a population by sampling a dataset with replacement. In essence, it helps the user to better understand the sampling distribution of a particular statistic from a collection of its own values arising from repeated samples (Singh and Xie, 2008). Bootstrapping was invented by statistician Bradley Efron in 1979 and has since allowed for a cheaper and more timely calculation of resampling statistics. The Bootstrap Resampling Method is based on the probability theory of the law of large numbers. This law states that with enough data, the empirical distribution of a sample will be a good approximation of the true distribution. As such, the higher number of resamples, the more accurate the results. Therefore, 100,000 resamples was chosen for use within this study because it is correlated with high accuracy and is the same number of resamples used in Olsen (2018). Because of the large number of resamples, computer software is used to conduct bootstrap. For this study, MATLAB software was utilized.

A major application of the statistical resampling technique is in the determination of confidence intervals (CI). This helps in answering questions regarding the CI of a

37

mean, median, or interquartile. Bootstrapping is better understood when applied to an example. Consider the following from Henderson (2005): the true value of a population is θ, where a set of n values are randomly sampled. The sample estimate $\hat{\theta}$ is based on the n values $(x_1, x_2, ..., x_n)$. Sampling with replacement, the n values now become the bootstrap sample $(x_1^*, x_2^*, ..., x_n^*)$. The bootstrap sample estimate θ^* is based upon the number of times the bootstrap sample is resampled. The higher the number of resamples, the higher the accuracy in the estimate. The exact number of resamples required to produce an accurate bootstrap resample is unknown, but is dependent on the sample size. Numerous studies have been accomplished in order to establish this ideal number of resamples. As a rule of thumb, larger datasets ($n \geq 50$) generally require a thousand or more bootstraps (Henderson, 2005). Ultimately, the more resamples, the more accurate the resulting data. The fundamental idea of bootstrap is similar to the Monte Carlo approximation, that states the sampling distribution $\theta^* - \hat{\theta}$ behaves like the sampling distribution $\hat{\theta} - \theta$ (Henderson, 2005).

For this study, each case from the final dataset was assigned a number from 1 to 102. The case numbers were then randomly sampled 102 times to create the bootstrap sample. Next, a total of 100,000 bootstrap samples were created by repeating this process. A statistical analysis was then run on each sample to generate the 95% CIs for each forecast metric, providing the mean, median, and interquartile ranges. The resultant error bounds give a good approximation of the true data distribution.

IV. Analysis and Results

This chapter presents the results obtained from applying the lightning prediction methods from Gremillion and Orville (1999) and Travis (2015) onto the Utah dataset.

Gremillion's method includes the use of only traditional/non-DP parameters, while Travis' method contains both traditional and DP variables. Gremillion's highest performing method for CCAFS/KSC is $Z \geq 40$ dBZ, for two consecutive volume scans, at the $-10°$C thermal height. Travis, however, found that $Z \geq 36.5$ dBZ with Z_{DR} at the $-10°$C thermal height was more superior in terms of lead times and lightning detection. After applying both methods and calculating forecast metrics and lead times, the results of Travis' method applied to the Utah dataset is compared to the findings in Olsen (2018). Olsen applied Travis' method to the Washington, D.C. area, where it was concluded that lightning prediction methods could not be applied universally. Olsen suggested expanding the research into new geographical regions.

The following analysis describes in detail a sample case from the dataset and a comparison of the Utah results to Gremillion and Orville (1999), Travis (2015), and Olsen (2018). An optimization for Z and Z_{DR} is also conducted to unveil the optimal threshold for each radar parameter that maximizes hits and minimizes FAs. Additional findings are also presented that were discovered during the course of the research. These newfound results may lead to additional research opportunities that could ultimately bolster lightning prediction methods and improve personnel safety.

4.1 Sample Case

To understand the results of this study better, an example case from the final dataset is presented. Figure 15 shows the GR2Analyst base reflectivity and the circled cell of interest. The cell formed 95 km north of KICX at 1730 UTC on 11

39

August 2015 and dissipated at 1815 UTC. The cell reached a maximum Z of 50 dBZ. After confirming it fell within the bounds of the southern testing area, the $-10°C$ thermal height was calculated. The $-10°C$ height was found to be 10,562 ft after applying the elevation correction. Once the thermal level of interest was established, radar interrogation efforts began using the cross-section and volumetric tools.

The cross-section tool was first utilized to examine the cell and determine whether or not it contained the Z and Z_{DR} values from Travis (2015). The position and swing functions were also used to adjust the radar cross-section and examine the entire cell. Figure 16 shows the (a) GR2Analyst volumetric Z display set to 36.5 dBZ and (b) the Z cross-section. The $-10°C$ thermal height was then overlaid onto both images
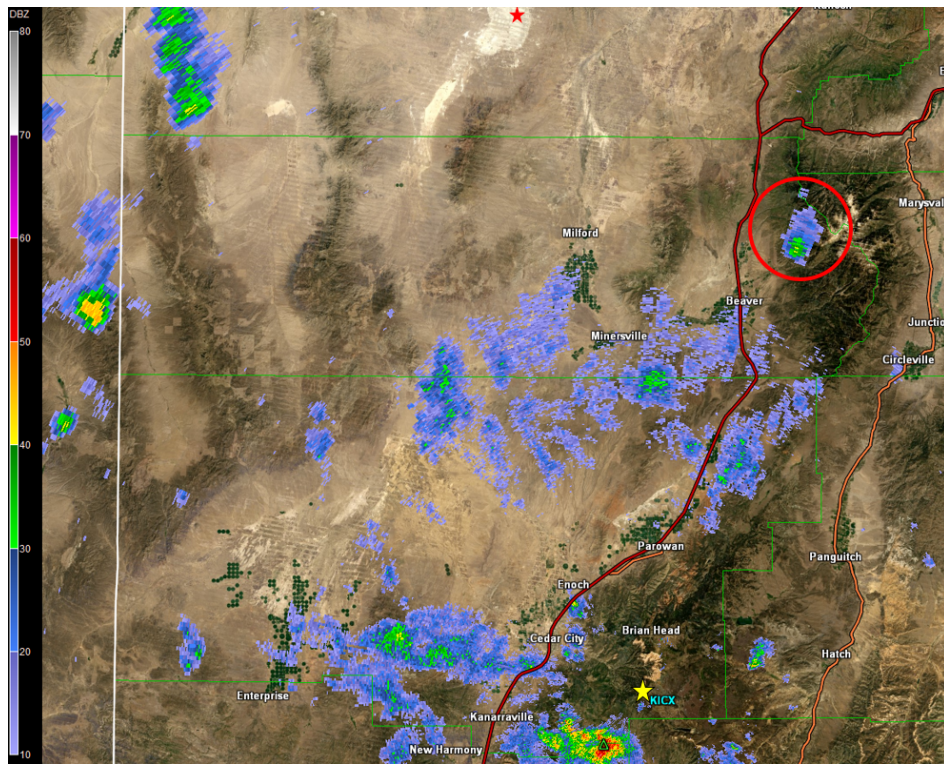
Figure 15. A radar image from GR2Analyst showing the base reflectivity on 11 August 2015, from KICX radar. The red circle indicates the cell of interest, the red star denotes the center of the TA LMA, and the yellow star is KICX radar. Image produced in GR2Analyst.

40
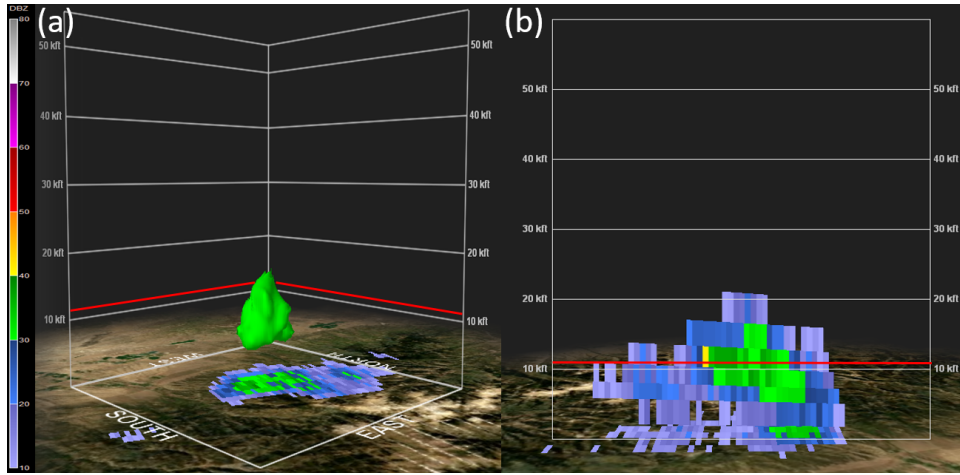
Figure 16. (a) Volumetric representation of Z with isosurface set to 36.5 dBZ; (b) cross-section of the same cell indicating the vertical extent of Z on 11 August 2015. The red lines in both images represent the $-10°$C thermal height. Images produced using GR2Analyst.
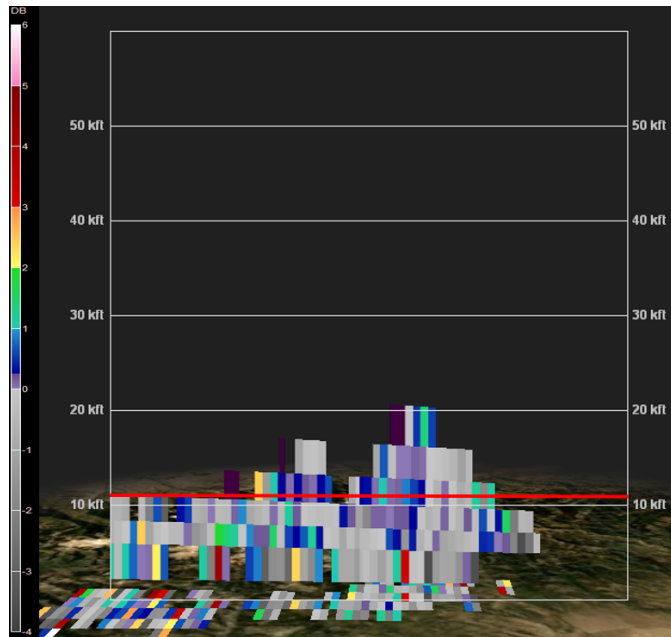
Figure 17. Z_{DR} radar cross-section showing the vertical distribution of Z_{DR} on 11 August 2015. The red line denotes the $-10°$C thermal height. Image produced in GR2Analyst.

41

to determine if the required thresholds were met here. The time when the 36.5 dBZ threshold was met at the red line in Figure 16 was recorded into the spreadsheet. For this case, Travis' Z threshold was met at 17:40:30 UTC. Z_{DR} was next examined using the same process. Figure 17 shows the Z_{DR} cross-section of the cell of interest. The ≥ 0.31 dB Z_{DR} threshold was met at the $-10°$C thermal height at 17:30:56 UTC and recorded as such into the spreadsheet. After both radar threshold times were recorded into the spreadsheet, Gremillion's lightning prediction method was next tested.

Gremillion's method was tested identically to Travis' method, except for the step of analyzing Z_{DR}. Using the same cell, GR2Analyst was employed to create a Z cross-section. Since the analysis was just complete using Travis' method, the step of creating a volumetric display was omitted, because the range of Z values was already known. Applying the same $-10°$C thermal height to the cross-section, the first instance of ≥ 40 dBZ was noted. Using the 'Next Volume Scan' button in GR2Analyst, the Z cross-section was then cycled to the next volume scan. Figure 18 illustrates the two consecutive Z cross-section volume scans in which Gremillion's lightning thresholds were met. The second instance of ≥ 40 dBZ at the $-10°$C height was recorded into the spreadsheet into a separate column from Travis' information.

Southwest Utah Forecast Outcomes

Lightning DNE	Lightning Occurrences	Total Cases
66	36	102

Travis Method

Hit	Miss	CR	FA
23	13	10	56

Gremillion Method

Hit	Miss	CR	FA
9	27	32	34

Table 2. **Summary of the forecast outcomes utilizing both Travis' and Gremillion's highest preforming lightning prediction methods and the total number of cases containing lightning-producing cells.**

42
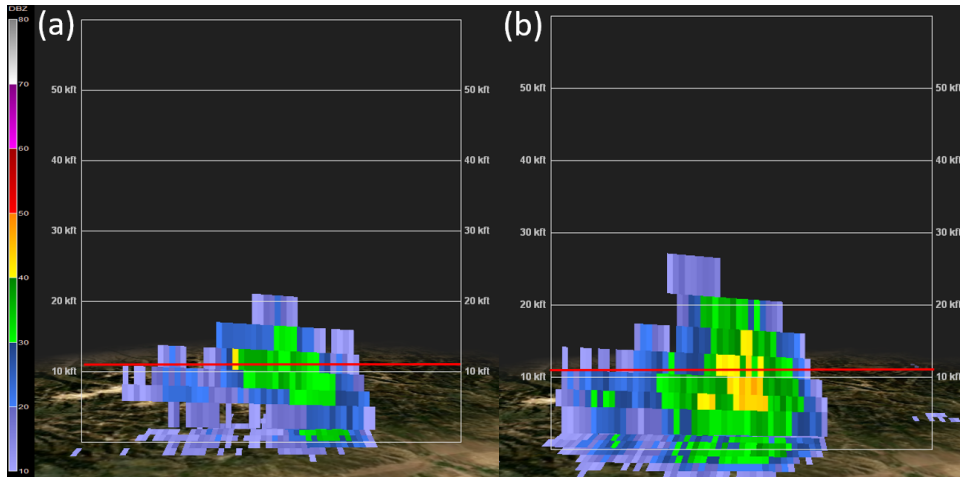
Figure 18. *Z* **radar cross-section employing the highest-preforming lightning prediction method from Gremillion and Orville (1999) across two consecutive volume scans. The first image (a) indicates the first instance where the** ≥ 40 **dBZ threshold was met. The second consecutive volume scan (b) shows identical** *Z* **values at the thermal height of interest. The red line denotes the** -10°**C height. Images produced in GR2Analyst.**

Once the times of both radar thresholds were recorded, MATLAB was used to establish the time of the first lightning discharge from the cell. Utilizing the LMA file containing the entire 45 min lifespan of the cell, MATLAB code was ran and programmed to stop at the time of the first lightning strike. This was accomplished by inserting latitude and longitude coordinates containing each cell. Each coordinate was recorded into the spreadsheet as either 'south latitude', 'north latitude', 'west longitude', or 'east longitude'. These coordinates were then ingested into MATLAB 'for loops' and ran against the LMA files using the methodology described in Section 3.3. The time of lightning occurrence was recorded as the time of lightning initiation in the spreadsheet. For Travis' method, this case was labeled a hit, because both radar parameters were met 22 min prior to the first lightning strike. Gremillion's method also produced a hit, but with only 17 min of lead time. Table 2 summarizes the forecast outcomes for Utah using both lightning prediction methods and the total number of lightning producing and non-lightning producing cases in the dataset.

43

4.2 Travis (2015) Comparison

This section describes the results of applying Travis' method to southwest Utah. It also compares the Utah results against Travis' results for CCAFS/KSC. This is accomplished by comparing and contrasting the forecast metrics and lead times from the two studies, and describing differences and similarities.

The forecast metrics of this study, as compared to the CCAFS/KSC area from Travis (2015), are the primary means of determining the forecast skill of Utah DP lightning prediction methods. Table 3 lists the computed forecast metrics for southwest Utah and CCAFS/KSC. The numbers in bold red indicate the least-performing forecast metric among the two locations. The first forecast metric, POD, resulted in undesirable results for the southwest Utah area. Used to calculate the probability of lightning detection, a POD of 1.0 is considered optimal. The POD for southwest Utah did not achieve favorable results, with a score of 0.6389. This means that 63.89% of the time, Travis' method was accurately predicting lightning onset in southwest Utah. This was less than Travis' POD of 0.8889, which shows that his method has a higher hit rate in the CCAFS/KSC area. The next metric, FAR, detects the skill of the forecast based on FAs. Utah's result was on the order of 12 times higher than CCAFS/KSC, suggesting FAs are the dominant forecast outcome. At 0.7089, this was a significant difference to the 0.0588 FAR calculated for CCAFS/KSC. PFA is an additional metric used to quantify FAs. For southwest Utah, PFA was 0.8485, which was again much higher than Travis' PFA of 0.0769. This result was somewhat expected, given both the high number of FAs from Table 2 and the high FAR from before. Next, TSS was calculated. This forecast metric accounts for all possible forecast outcomes in the calculation and is a good indicator of overall forecast skill. A TSS of 0.2096 resulted for southwest Utah, which was approximately four times less than Travis' TSS of 0.8120. A TSS of 1.0 indicates perfect skill, whereas a score of 0.0

44

Southwest Utah and CCAFS/KSC Forecast Metrics

	Southwest Utah	CCAFS/KSC
POD	0.6389	0.8889
FAR	0.7089	0.0588
PFA	0.8485	0.0769
TSS	-0.2096	0.8120
CSI	0.2500	0.8421
Mean OUI	0.2891	0.7504
Median OUI	0.2561	0.7067
Mean OUI*	0.2734	0.7111
Median OUI*	0.2467	0.6848
Mean OUI†	0.2891	0.7504
Median OUI†	0.2561	0.7067

Table 3. Overview of the forecast metrics computed using Travis' lightning prediction method in southwest Utah and CCAFS/KSC. The red-colored numbers indicate the worst performing forecast metric as compared to the other location.

indicates no forecast skill. The -0.2096 TSS for Utah suggests that Travis' method was better at forecasting non-lightning events rather than actual lightning producing cells. The last standard forecast metric, CSI, was calculated in order to provide additional insight into the lightning prediction forecast method. A CSI of 0.2500 was computed for southwest Utah and a CSI score of 0.8120 for the CCAFS/KSC area. Similar to previous metrics, this Utah metric was much worse than Travis' scores. At exactly one-quarter of the optimal score, Utah's CSI indicates poor overall performance of predicting critical events. Utilizing the bootstrapping method, 100,000 resamples were created in MATLAB from the original 102 cases in the final dataset. The resultant 95% CIs were plotted with each forecast metric. Figure 19 shows the five forecast metrics with 95% CI for both the southwest Utah and CCAFS/KSC areas. Almost all of the Utah forecast metrics were statistically different from Travis' metrics, except for POD. This was made evident by the slight overlap in the 95% CI bounds. Interestingly, this result was identical to Olsen (2018), where the author found that the POD for Washington, D.C. and CCAFS/KSC were also similar.

45
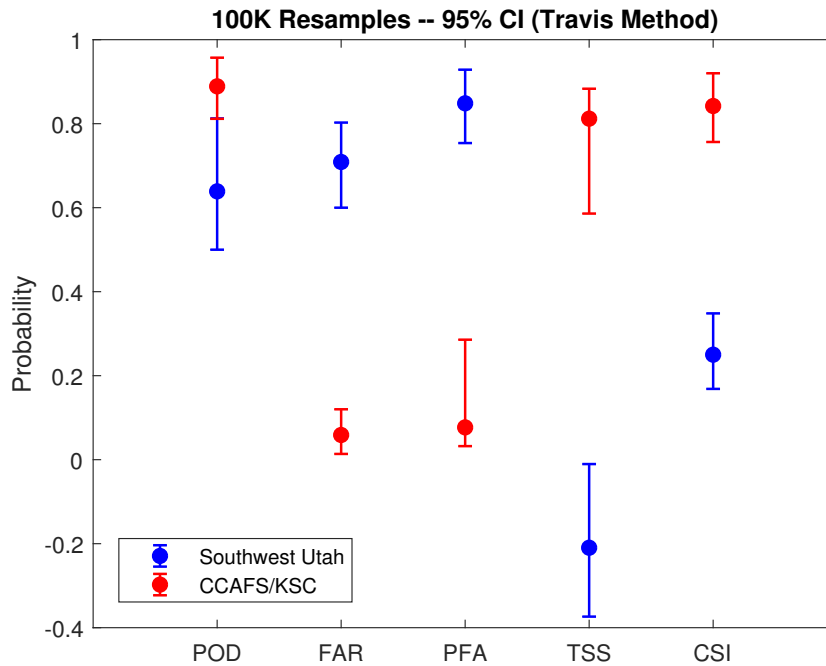
Figure 19. All five forecast metrics resampled 100,000 times using bootstrapping with 95% CI for the southwest Utah and CCAFS/KSC area. Each forecast metric indicated that they were statistically different between the two locations, except for POD which had slight overlap in the 95% CI bounds. Image produced in MATLAB.

The next three forecast statistics calculated are the nonstandard metrics mentioned in Chapter III: OUI, OUI*, and OUI†. Primarily used to test the operational utility of lightning initiation prediction algorithms for the 45 WS, each forecast metric differs in a variation of the lead time term. As such, differences among the three metrics are small. In fact, it was recently proven that there is no significant difference in OUI and OUI*. In Nava (2018), recomputing Travis' original OUI to the OUI* metric showed similar results between the two metrics. The lead time term is weighted at two and is one of three other forecast metrics used in the overall calculation. Figure 20 shows the three versions of OUI and their corresponding 95% CIs. For this study, the original mean OUI from Travis (2015) applied to the Utah dataset resulted in a score of 0.2891, which was much less than the CCAFS/KSC value of

46
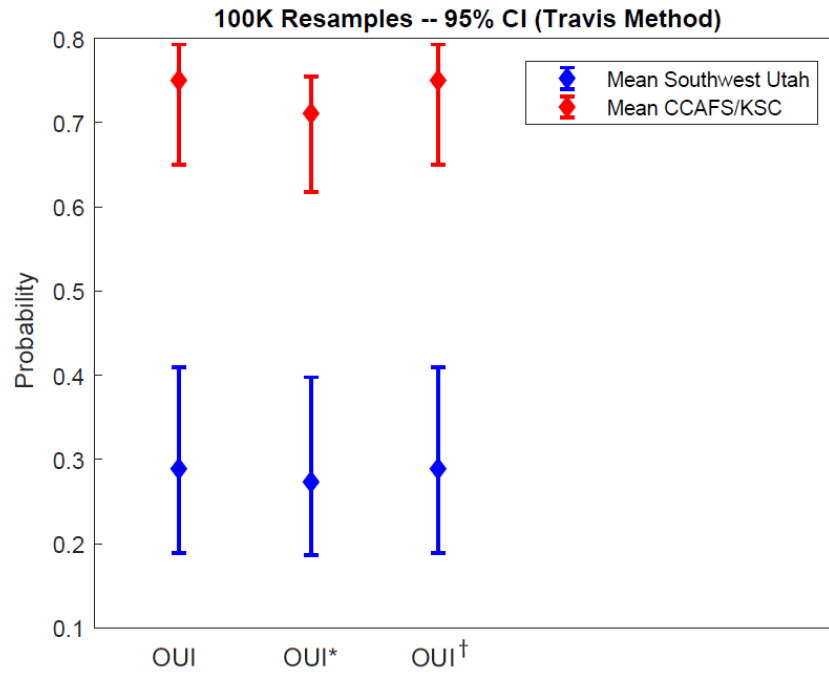
Figure 20. The three modified versions of OUI for both the southwest Utah and CCAF-S/KSC area. OUI† had the highest scores for both southwest Utah and CCAFS/KSC. Image produced in MATLAB.

0.7504. The first modified version, OUI* from Olsen (2018), produced a worse score for Utah and CCAFS/KSC, at 0.2734 and 0.7111, respectively. Both reductions were expected with the use of the maximum lead time, which increases the size of both denominators. The final modified OUI was OUI†. For Utah, the score improved to 0.2891, which was the same as OUI. CCAFS/KSC also remained the same as the original OUI at 0.7504. This was due to the cap placed upon the maximum lead time term in the OUI† calculation. Further comparisons with Olsen (2018) and Gremillion and Orville (1999) are needed to prove which OUI produces the highest scores.

After all Utah forecast metrics were calculated and compared with CCAFS/KSC, the lead time calculations from Travis (2015) were next analyzed. Table 4 shows the mean, median, and maximum lead times for Travis' method applied to the two testing sites. The mean lead times between the two locations favor CCAFS/KSC

www.manaraa.com

Southwest Utah and CCAFS/KSC Lead Times

	Southwest Utah	CCAFS/KSC
Mean Lead Time (mins)	9.9565	11.8372
Median Lead Time (mins)	6.0000	6.6000
Maximum Lead Time (mins)	37.0000	49.8167

Table 4. The mean, median, and maximum lead times using Travis' lightning prediction method for southwest Utah and CCAFS/KSC. The red text indicates the less-than-favorable metric as compared to the other location.
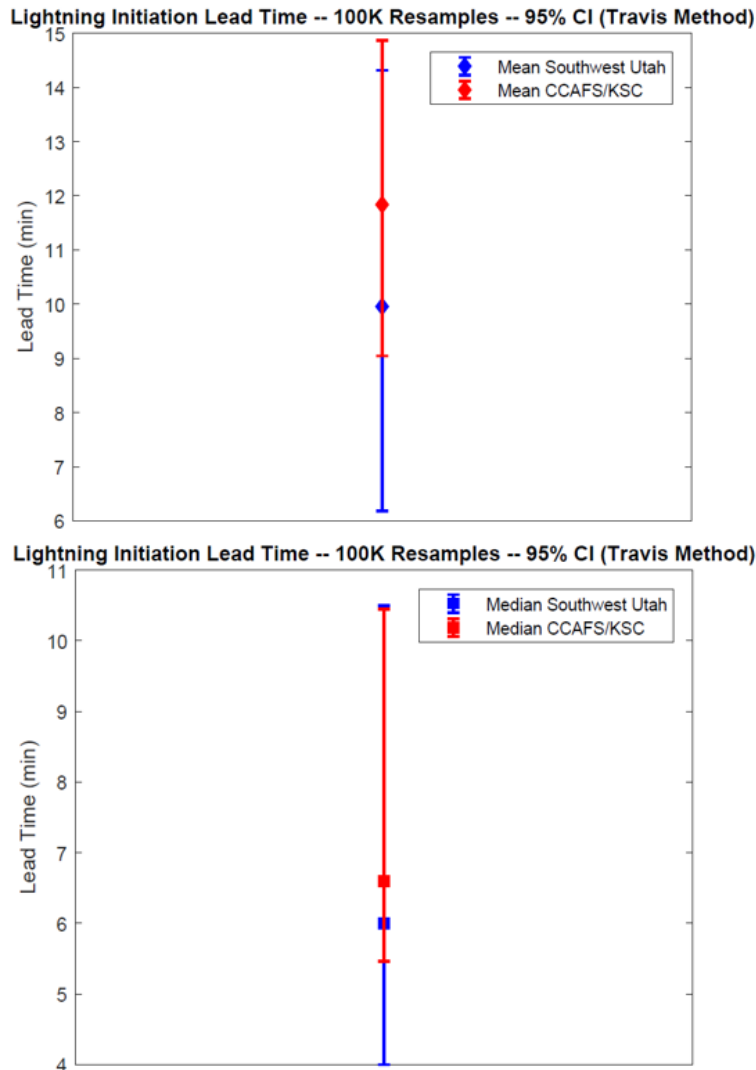
Figure 21. The mean and median lead times for southwest Utah and CCAFS/KSC. Both locations have statistically similar results, but CCAFS/KSC has a higher mean CI. Images produced in MATLAB.

48

by approximately 2 min. Both median lead times, however, were much more similar with less than a tenth of a difference between the two regions. Maximum lead time was also different, with Travis' study indicating 50 min and less for Utah at 37 min. Figure 21 shows the mean and median lead time differences, with 95% CIs. The 95% CIs were computed using the same bootstrap resampling technique as before. The overlapping CI bounds indicated that despite different mean, median, and maximum lead times, the lead times are generally alike. This was unexpected, due to the vast differences between the two areas. However, this result may suggest that lightning forecast lead times are similar across all regions, regardless of method or climate.

4.3 Olsen (2018) Comparison

The second comparison conducted in this study compares the results of the Travis method in Utah against the findings in Olsen (2018). Olsen focused on applying Travis' lightning initiation thresholds to the Washington, D.C. area. By comparing Olsen's D.C. findings to the Travis Utah results, it can provide insight into DP lightning forecast method performance in different regions. Similar to before, this section details the eight forecast metrics with 95% CIs and the lead time calculations.

All eight forecast metrics for Utah were inferior to the Washington, D.C. study. Table 5 provides an overview of all eight metrics, for both the southwest Utah and Washington, D.C. locations. The Utah POD was 0.6389, which was slightly lower than the POD from Olsen (2018) at 0.7222. Though Utah's POD was lower, it is worth noting that both locations were more similar to one another than Utah and CCAFS/KSC in the Travis comparison. The FAR for Utah was also higher than the other study, at 0.7089 compared to Olsen's 0.5000. PFA and TSS were among the worst performing forecast metrics. Both figures were much worse than the Washington, D.C. study, likely because of the vast terrain and elevation differences

49

between the two regions. CSI performance statistics were also more similar than in the Travis comparison, where there was a difference of nearly four times the Utah value. Both CSI scores were low, indicating that Travis' method has poor skill in predicting the occurrence/non-occurrence of lightning in Utah and Washington, D.C.

Figure 22 shows the 95% CI for the five forecast metrics. Almost all of the forecast metrics for southwest Utah had comparable results to Washington, D.C., as indicated by the overlapping CIs. PFA and TSS were the only two metrics that were statistically different. An interesting result was that Olsen (2018) had similar findings when Washington D.C. was compared to CCAFS/KSC. Olsen found POD and PFA to be statistically similar, while FAR, TSS, and CSI different. It was not surprising for Utah's TSS to be the worst performing TSS among the three locations. This was made evident by it being the only negative scoring TSS, suggesting little-to-no forecast skill. This likely resulted from the significant elevation and climate differences among Utah, CCAFS/KSC, and Washington, D.C. Both of these east coast sites are located at sea level. This is in stark contrast to Utah, where the elevation ranges

Southwest Utah and Washington, D.C. Forecast Metrics

	Southwest Utah	Washington, D.C.
POD	0.6389	0.7222
FAR	0.7089	0.5000
PFA	0.8485	0.4063
TSS	-0.2096	0.3160
CSI	0.2500	0.4194
Mean OUI	0.2891	0.5311
Median OUI	0.2561	0.4990
Mean OUI*	0.2734	0.5108
Median OUI*	0.2467	0.4849
Mean OUI†	0.2891	0.5108
Median OUI†	0.2561	0.4849

Table 5. Overview of the forecast metrics computed using Travis' lightning prediction method in southwest Utah and Washington, D.C. The red-colored numbers indicate the worse-preforming forecast metric among the two locations.
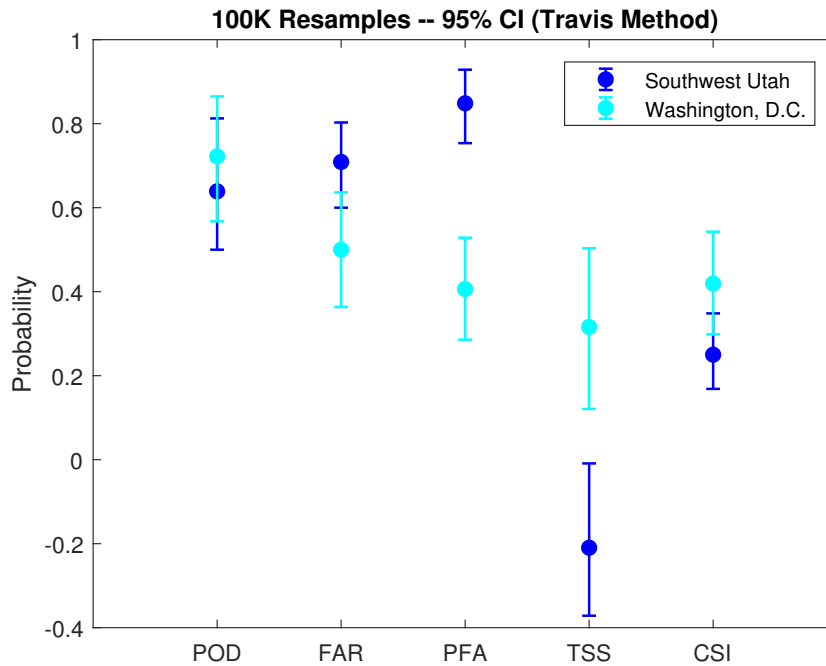
Figure 22. All five forecast metrics with 95% CI for the southwest Utah and Washington, D.C. area. The metrics indicate that POD, FAR, and CSI are statistically similar, while PFA and TSS are different. Image produced in MATLAB.

from 2,300 ft to over 13,500 ft. In addition, the climatic differences between these three locations are significant. CCAFS/KSC and Washington, D.C. both lay along the Atlantic Ocean, which allow for a mild, humid maritime climate. The primary weather drivers here are determined by synoptic-scale circulations and local sea/land-breeze interactions. Utah, on the other hand, is largely comprised of vast mountain ranges and continental dry desert. Weather in the summer is primarily determined by the onset and location of heat lows, which form as a result from the North American Monsoon. This seasonal feature peaks in strength during the late summer months and brings widespread thunderstorms and precipitation to the southwest United States.

The three OUIs were then compared to Olsen (2018) and Utah. Figure 23 shows the three OUIs, with 95% CI, for the southwest Utah and Washington, D.C. regions.
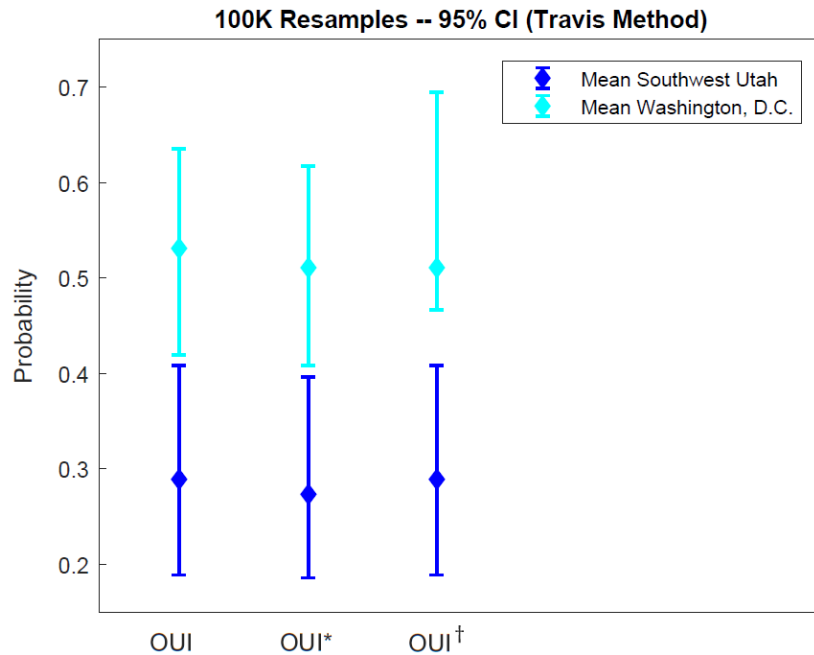
Figure 23. The three modified versions of OUI for both the southwest Utah and Washington, D.C. area. While OUI* was the highest for Utah, OUI† held the highest mean for both locations. Image produced in MATLAB.

As expected, Washington, D.C. had higher-preforming OUIs compared to Utah. Similar to the previous CCAFS/KSC OUI comparison, where they were each drastically different from one another, these forecast metrics were more alike. This was an interesting result because it indicated that Washington, D.C. and Utah produce more similar results than originally anticipated. The reason for this may stem from similarities in the aerosol load. Washington, D.C. is a highly-populated metropolitan area, which allows for high anthropogenic aerosol counts. Though Utah is not highly populated, it has high aerosol counts due to lofted dust. A high dust load can act as additional CCN and possibly induce thunderstorm formation in the right atmospheric conditions. This could also be true for highly-populated areas (i.e New York City, Atlanta, or Charlotte) due to the increased concentration of anthropogenic aerosols. In addition to aerosols, it is worth noting that both Washington, D.C. and

52

southwest Utah are approximately at the same latitude. It is unknown what exactly could be causing the heightened similarities in the data between the two testing sites, especially considering the vast terrain/climate differences and the large distance separating them. However, it is possible that multiple regions, regardless of climate or terrain, along the same latitude have similar lightning initiation criteria. The similarities could result from similar mid-latitude weather and climate regimes between Utah and Washington, D.C. While this theory appears to verify well for Utah and Washington, D.C., more research will be required to confirm or deny this theory.

The final comparison of Olsen (2018) to this study included an examination of lead times. Table 6 summarizes the mean, median, and maximum lead times for both locations using Travis' lightning prediction method. Similar to before, Utah's mean and median lead times were inferior to Washington, D.C. However, it is interesting to note that Utah and CCAFS/KSC had more similar mean and median lead times than Utah and Washington, D.C. This was made evident by the more similar mean and median lead times between Utah and CCAFS/KSC in Table 4. This suggests that Utah and CCAFS/KSC are composed of more similar duration airmass-type thunderstorms. The maximum lead times for Utah and Washington, D.C. were coincidentally the same at 37 min. The 95% CI intervals for both studies were also calculated. Figure 24 shows the median and mean lead times with their respective 95% CIs. Similar to the CCAFS/KSC comparison, significant overlap among the CIs indicate that the lead times were generally alike. It is also worth noting that the 95% CI bounds of Washington, D.C. are much wider than Utah, suggesting a more diverse range of lead times. This was different from the Travis comparison, where Utah and CCAFS/KSC were more statistically similar. This result confirms that Utah and CCAFS/KSC have more similar airmass-type thunderstorms than Washington, D.C.

Southwest Utah and Washington, D.C. Lead Times

	Southwest Utah	Washington, D.C.
Mean Lead Time (mins)	9.9565	12.8462
Median Lead Time (mins)	6.0000	9.0000
Maximum Lead Time (mins)	37.0000	37.0000

Table 6. The mean, median, and maximum lead times using Travis' method for southwest Utah and Washington, D.C. The red-colored text indicates the least amount of lead time among the two locations.
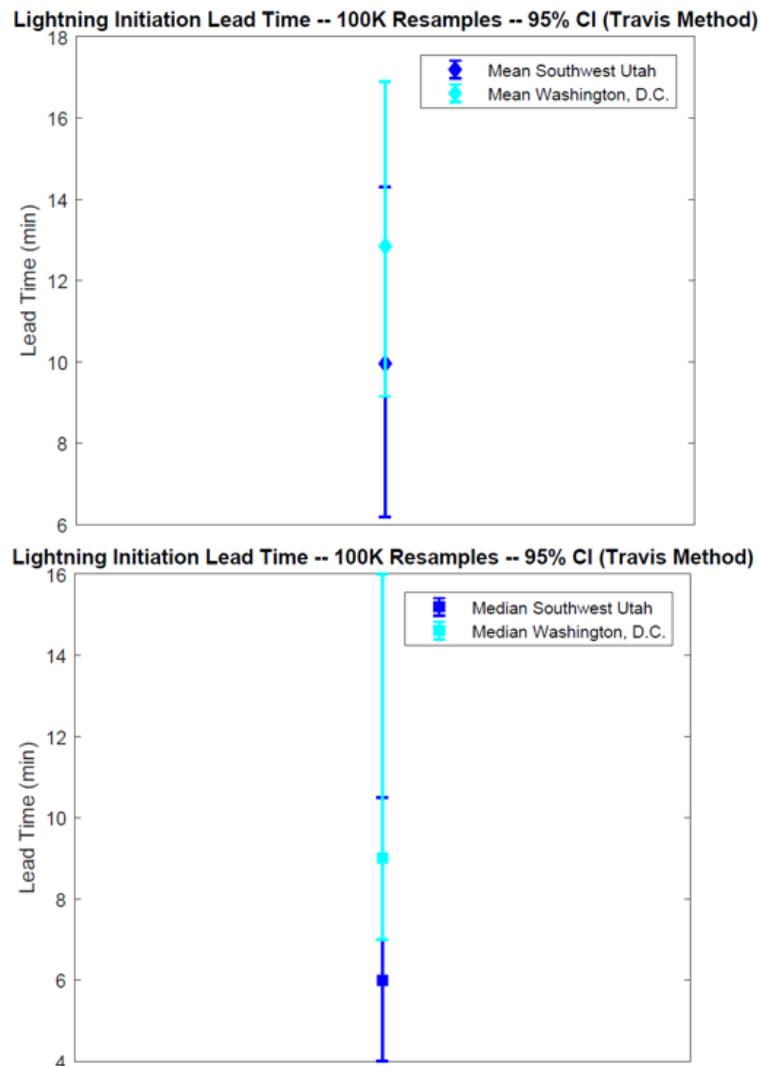
Figure 24. The mean, median, and maximum lead times for southwest Utah and Washington, D.C. Both locations had similar lead times, as made evident by the overlapping CIs. Images produced in MATLAB.

4.4 Gremillion and Orville (1999) Comparison

The final comparison in this study includes the traditional (i.e. non-DP) radar lightning initiation prediction technique described in Gremillion and Orville (1999). The highest preforming LIST, $Z \geq 40$ dBZ for two consecutive volume scans at the $-10°$C thermal height, from the study was tested on the final Utah dataset. By testing a traditional radar forecast method against a DP method, it can provide insight into its skill over DP lightning prediction and its spatial behavior. This is shown by computing the same eight forecast metrics from before, with 95% CIs, and comparing lead time differences. The Utah Gremillion method is compared against the Travis method for both the CCAFS/KSC and Washington, D.C. areas.
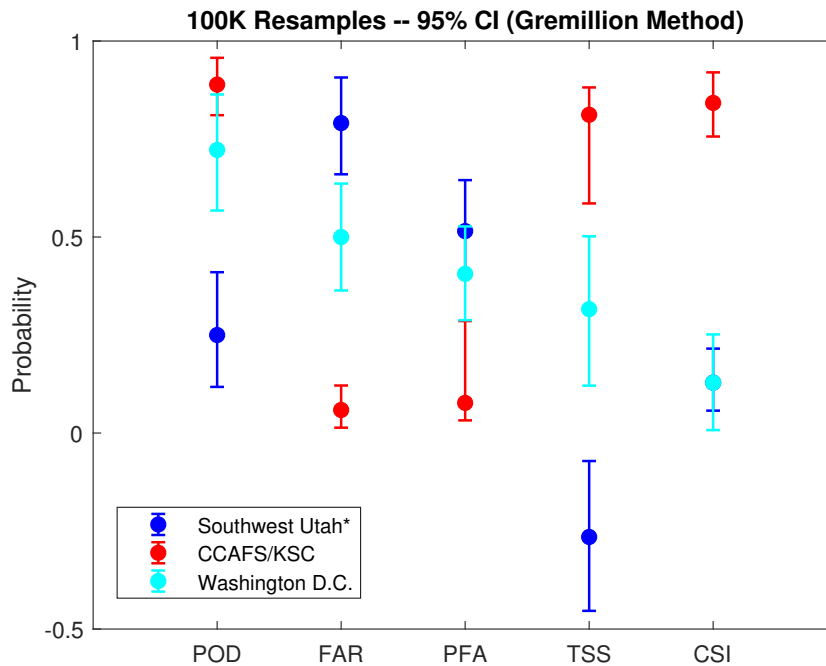
Figure 25. All five forecast metrics with 95% CI for the southwest Utah, CCAFS/KSC, and Washington, D.C. areas. The metrics for southwest Utah are based on Gremillion's highest-performing LIST, while the other two use Travis' forecast method. The metrics indicate that PFA and CSI are similar for both Utah and Washington, D.C. despite different forecast methodologies. Image produced in MATLAB.

55

Southwest Utah, CCAFS/KSC, and Washington, D.C. Forecast Metrics

	Southwest Utah*	CCAFS/KSC	Washington, D.C.
POD	0.2500	0.8889	0.7222
FAR	0.7907	0.0588	0.5000
PFA	0.5152	0.0769	0.4063
TSS	-0.2652	0.8120	0.3160
CSI	0.1286	0.8421	0.4194
Mean OUI	0.1751	0.7504	0.5311
Median OUI	0.1464	0.7067	0.4990
Mean OUI*	0.1848	0.7111	0.5108
Median OUI*	0.1529	0.6848	0.4849
Mean OUI†	0.1751	0.7504	0.5108
Median OUI†	0.1464	0.7067	0.4849

Table 7. The eight forecast metrics for the southwest Utah, CCAFS/KSC, and Washington, D.C. regions. The asterisk denotes the regions in which Gremillion's LIST was applied; all other locations are based on Travis' method. The red text indicates the less-than-favorable metric as compared to the other location.

Table 7 summarizes the eight forecast metrics calculated using Gremillion's LIST for southwest Utah and Travis' method for CCAFS/KSC and Washington, D.C. Similar to the two previous comparisons, southwest Utah had the worst scoring metrics among the three testing regions. Only one of the eight forecast metrics improved over Travis' method in Utah. Table 3 shows a PFA of 0.8485, which decreased to 0.5152 when Gremillion's method was applied. This result was somewhat expected, as the low Z threshold in Travis (2015) often resulted in FAs. A high number of FAs were the main issue with Travis' method in Washington, D.C. as well. (Olsen, 2018). However, raising the Z requirement to 40 dBZ in the Utah region may be too high, as the other seven forecast metrics worsened. Figure 25 shows the eight forecast metrics and their corresponding 95% CIs. It was interesting that, despite using different lightning forecast methodologies, PFA and CSI were identical for Utah and Washington, D.C. This suggests that Gremillion's method for Utah and Travis' method for Washington, D.C. perform equally ineffective in terms of FA occurrence and overall forecast skill.

56
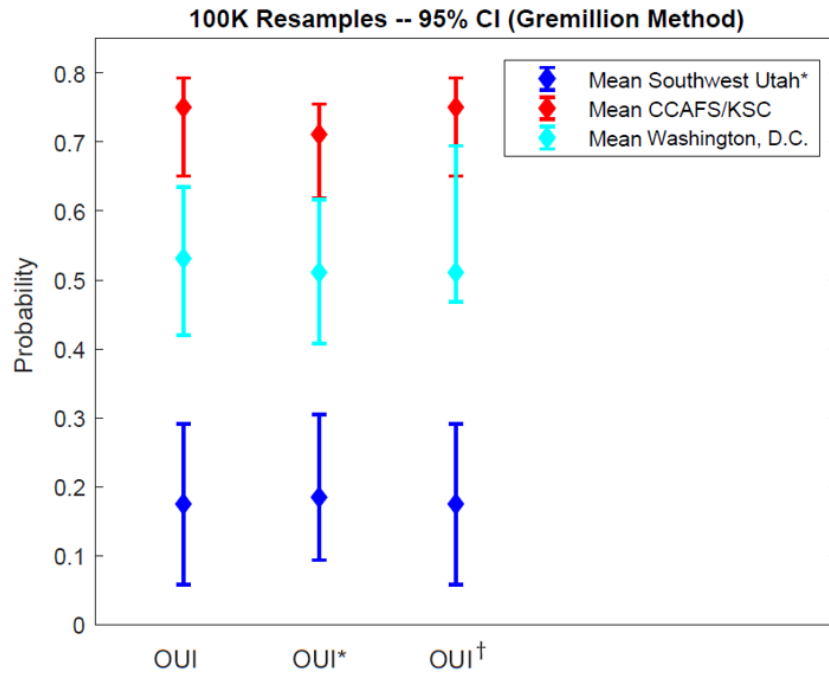
Figure 26. The three modified versions of OUI for all three locations. Southwest Utah's data was computed using Gremillion's LIST and the other two locations utilized Travis' method. Image produced in MATLAB.

The three OUIs were next compared to demonstrate overall operational utility of Gremillion's lightning prediction method for use in Utah. Figure 26 indicates the three mean modified OUIs with their corresponding 95% CIs. OUI*, in this case, had the highest mean for Utah/Washington, D.C. and its worst score for CCAFS/KSC. This resulted from CCAFS/KSC having the highest overall maximum lead time at 49.8167 minutes (Table 4). It is also important to note that Gremillon's method for Utah produced results that were statistically different from the other two locations.

Lastly, a comparison of lead times for the three locations was examined. Table 8 summarizes the mean, median, and maximum lead times for southwest Utah using Gremillion's method, and Travis' method for CCAFS/KSC and Washington, D.C. For the first time in this study, Utah did not have the lowest scoring forecast metric. The median lead time for southwest Utah was at 7.0000, which bested CCAFS/KSC by

Southwest Utah, CCAFS/KSC, and Washington, D.C. Lead Times

	Southwest Utah*	CCAFS/KSC	Washington, D.C.
Mean Lead Time (mins)	10.4444	11.8372	12.8462
Median Lead Time (mins)	7.0000	6.6000	9.0000
Maximum Lead Time (mins)	27.0000	49.8167	37.0000

Table 8. The mean, median, and maximum lead times using Gremillion's LIST for southwest Utah and Travis' method for CCAFS/KSC and Washington, D.C. The red-colored text indicates the worst lead time, as compared to the other locations.
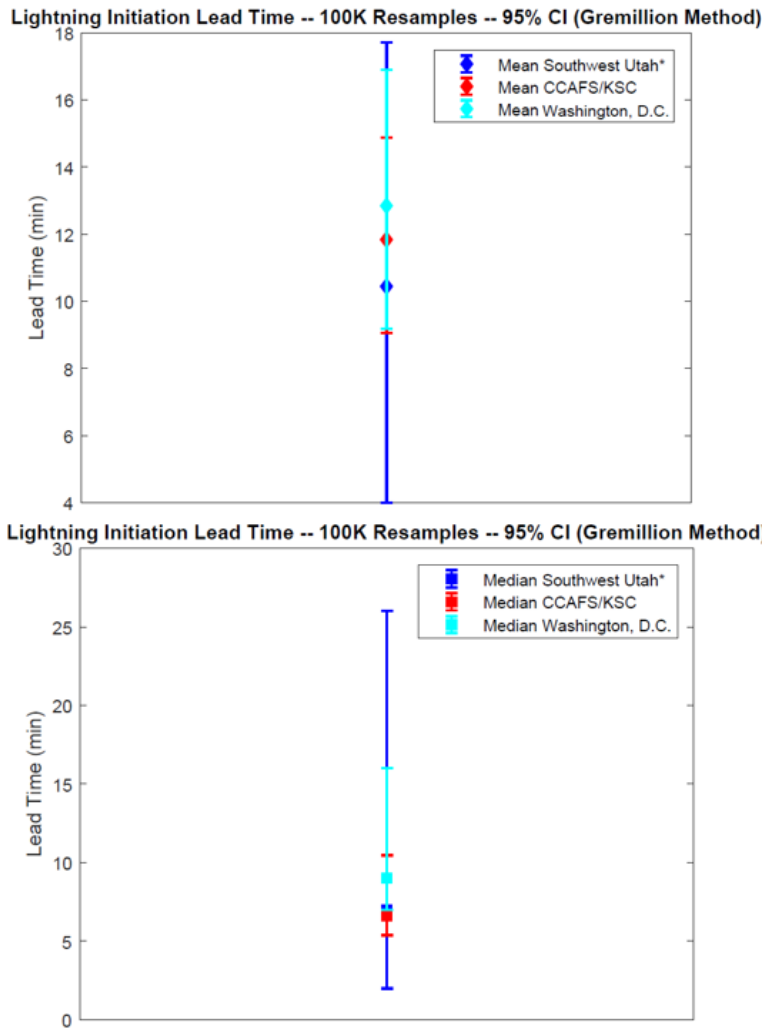
Figure 27. The mean and median lead times with 95% CI bounds for all three locations. All three locations were generally alike, despite different locations and lightning forecast methodologies. Images produced in MATLAB.

0.4000 minutes. Given the stricter requirements of the Gremillion method, where two consecutive volume scans are necessary, one would think this would result in lost lead time; however, the opposite was observed. Figure 27 shows the mean and median lead times for each location, with their 95% CIs. More information regarding the spread of the data can be inferred from this plot. Southwest Utah had the largest extent of lead times. The close proximity of the median lead times of Utah and CCAFS/KSC was also interesting, as this finding was similar to the Travis Utah dataset, where both locations' medians were within a minute of one another. The similar medians of Utah and CCAFS/KSC further suggests similar airmass-type thunderstorms between the two locations. This is in contrast to the Washington, D.C. area, where synoptically-driven multicellular thunderstorms are more common than airmass thunderstorms.

4.5 Additional Findings

This section focuses on some of the additional findings that were made evident while analyzing the main research objective. This includes the range of Z and Z_{DR} values for cells in the final dataset, the occurrence/non-occurrence of lightning in unusual atmospheric conditions, and an optimization of Z and Z_{DR} LIST thresholds.

4.5.1 Reflectivity

During the process of thunderstorm cell interrogation, it was observed that Travis' Z_{DR} threshold requirement was met in every case and with considerably more lead time than Z. This result was similar to Olsen (2018), where it was discovered that Z_{DR} was always met prior to or at the same time as the Z threshold. Olsen stated that Z was the determining factor as for whether or not a cell produced lightning. The reason for Z_{DR} preceding Z stems from the interactions of graupel, ice, and water particles during the early stages of thunderstorm development. The Z_{DR} radar

59

product easily differentiates between these spherical and non-spherical hydrometeors during the collisions and coalescence stage. This is in contrast to Z, which requires a much larger target to scatter enough reflected energy back to the radar antenna. These reflections do not usually occur until large rain drops or hailstones are present in the thunderstorm and well after the first lightning strike. The findings from this study concur with Olsen (2018) that Z is the determining factor for Utah lightning. Z_{DR} will be analyzed in the next section to determine the optimal value for Utah.

In GR2Analyst, the highest Z and Z_{DR} values were recorded for each cell. For lightning producing cells, this value was defined as the 'instantaneous' Z or Z_{DR} value; non-lightning producing cells were defined as the 'highest' Z or Z_{DR} values. Instantaneous radar thresholds are explained as the largest Z or Z_{DR} value in the cell during actual lightning discharge at zero lead time. Table 9 shows the mean Z value for non-lightning producing cells and lightning producing cells. The difference between the two Z means was less than a tenth of one dBZ. This conveys the difficulty in choosing a Z threshold that can accurately predict the occurrence of Utah lightning.

Another interesting observation noted from the research study was the extent of Z values for both non-lightning and lightning producing cells. Figure 28 shows histograms for both scenarios on the southwest Utah final dataset. The range of Z values for both lightning and non-lightning occurring cells was interesting, as there are numerous cases where lightning occurred despite $Z \leq 30$ dBZ. This was an unanticipated result because most radar/lightning studies show $Z \approx 35$ dBZ at the $-10°$C

Mean Southwest Utah Reflectivity

Mean Highest Z		Mean Instantaneous Z	
Lightning DNE	38.697 dBZ	Lightning Occurs	38.725 dBZ

Table 9. The mean highest Z recorded in non-lightning producing cells and the mean instantaneous Z in lightning producing cells. The highest Z value is defined as the highest recorded dBZ value for a non-lightning producing cell. Conversely, the instantaneous Z is the largest reflectivity value at the time of lightning initiation.
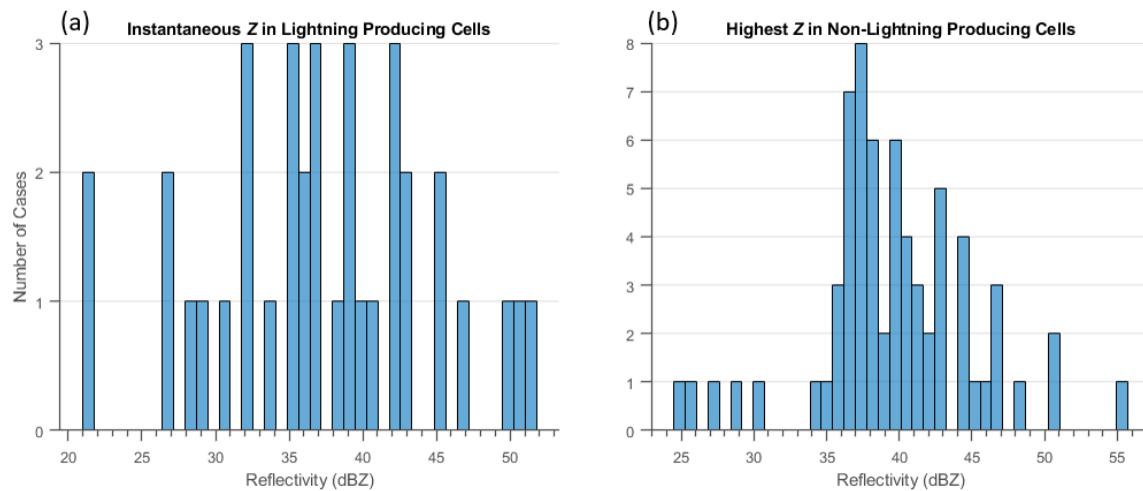
Figure 28. Histograms showing (a) the instantaneous Z in lightning producing cells and (b) the highest Z in non-lightning producing cells. The overall average Z was 38.711 dBZ, with (a) averaging 38.725 dBZ and (b) averaging 38.697 dBZ. The range of overall Z shows the difficulty in narrowing down a single Z threshold for use in Utah lightning prediction methods. Images produced in MATLAB.

height provides the best performance regardless of location (Yang and King, 2010). Analyzing these peculiar results further was necessary in order to determine the cause.

Radar and LMA coverage were both first re-examined to ensure that the $Z \leq 30$ dBZ cases fell within bounds of both sensors. After verifying they met the final dataset criteria, both sensor statuses were also checked to confirm they were both fully operational. Next, the locations of the cells were plotted using MATLAB to see if the cells were forming in a similar area or along a particular terrain feature. This revealed that the cells had a spatial pattern south of the TA LMA, in an area characterized by a large dry lake bed. The researcher then began to look into the potential impacts of dust on cell formation by downloading past weather observations.

IEM (2018) was utilized to download historical weather observations across four different airports nearest the dry lake bed area for the dates when lightning occurred with $Z \leq 30$ dBZ. It was found that for each day, there were gusty wind conditions reported at each observing location from the southwesterly direction, across the lake

61

bed. The researcher hypothesizes that the increased wind speeds lofted dust into the air from the dry lake bed, thus allowing the foreign aerosol to act as CCN. This, in turn, expedited the thunderstorm charging process and allowed lower Z values to correspond to lightning. This theory is supported by a Saharan dust impact study on convective clouds in Koren et al. (2005), where it was discovered that the presence of dust aerosols correlate strongly with the structural properties of convective cloud features. This was caused by the large abundance of aerosols acting as additional CCN, enabling more numerous and smaller cloud droplets to grow through the collisions and coalescence process (Koren et al., 2005). This same type of aerosol invigoration may have occurred in Utah and explain why lower Z values correspond to lightning.

Perhaps the most puzzling result of this study were the few cases where cells containing $Z \geq 45$ dBZ did *not* produce lightning. This finding was examined further using the same process described above; however, no spatial pattern, nor any seasonal/time dependence was observed in the data. The elevation impacts on thunderstorm development were next considered. As noted in Chapter II, the electric field level required for lightning discharge at 6 km altitude is approximately 1/3 of what is required at sea level (Rakov and Uman, 2003). This is due to the decreased air pressure, which increases droplet size. It is possible that there are unknown impacts of the high Utah elevation environment on large droplet behavior within thunderstorms. Or perhaps there was another meteorological or non-meteorological component involved in the charging process that was acting as an insulator, ultimately restricting the lightning strike. However, investigating this concept further is beyond the scope of this study.

The large spread of Z values for both lightning and non-lightning producing cells indicates the difficulty in forecasting Utah lightning initiation. Travis' Z threshold outperformed Gremillion's Z requirement only because it was lower and required one

Southwest Utah Z Performance

Z Value (dBZ)	Hit Rate	FA Rate	TSS
35	0.6111	0.8082	−0.2828
35.5	0.5555	0.7368	−0.2929
36	0.5555	0.7368	−0.2929
36.5	0.4722	0.7424	−0.2547
37	0.4722	0.7258	−0.2095
37.5	0.4722	0.7068	−0.1489
38	0.4444	0.6862	−0.0858
38.5	0.4444	0.6800	−0.0707
39	0.3611	0.7173	−0.1388
39.5	0.3333	0.6923	−0.0757
40	0.3333	0.6756	−0.0454
40.5	0.3055	0.6764	−0.0429
41	0.3055	0.6451	+0.0025
41.5	0.3055	0.6451	+0.0025
42	0.2222	0.6923	−0.0505

Table 10. A tabular summary indicating the hit rate, FA rate, and TSS for different Z thresholds. Note: The hit rate and FA rate are not the same as POD and FAR, respectively. They are values obtained from counting the number of hits, misses, CRs, and misses using histogram data obtained from Figure 28.

volume scan. If Gremillion's Z parameters were reduced and lowered to one volume scan, it would have likely produced better results. This idea serves as the basis of improving the performance of a new Z prediction threshold and optimizing it for the Utah region. Table 10 shows the tabular summary of the hit rate, FA rate, and TSS score for 15 different Z thresholds. The hit rate and FA rate are calculated the same as POD and FAR, respectively. However, they are named differently because of the process used to tabulate the number of hits, misses, and CRs from histogram data obtained in Figure 28. Calculating forecast metrics using histogram data provided a rough optimization of the data because it contains error associated with the assumptions used in creating both histograms. For example, the instantaneous Z may not be the actual Z during discharge, as it was instead recorded as the closest Z to the actual lightning strike. This occurred because the radar volume scan did not always

occur exactly at the same time of the first lightning strike. As such, the actual instantaneous Z value could be higher or lower than the closest recorded time. A small amount of experimental error resulted using this method and continued to propagate as the data was further manipulated. Nonetheless, the chosen method provides a generalized optimization of Utah Z thresholds acceptable for forecasting purposes.

Figure 29 shows the hit rate and FA rate columns from Table 10 plotted onto a scatter plot, with a least squares fitting power law curve. Hit rate decreased more steeply with increasing Z; FA rate also decreased with Z, but more linearly than hit rate. The 38 dBZ threshold, where the hit and FA rates are half-way to their minimums, may be the optimal Z value because it is balanced in terms of maximizing hits/minimizing FAs. Because the hit rate directly corresponds to personnel safety, most forecast units will err on the side of safety and opt for a lower Z value. However, the high number of FAs that result from a low Z value can also evolve into a safety issue. This is because too many FAs over time can reduce the seriousness of an issued lightning watch and ultimately reduce forecast credibility for the issuing organization. If this becomes the case, operators may not heed necessary safety precautions when lightning watches and warnings are issued, putting them at risk. Utah is one example of a location where FAs need to be regarded equally with hits when considering safety.

One additional statistic that can be utilized in determining the optimal Z value is TSS because it indicates how well a method performs at predicting the occurrence or non-occurrence of an event (Joliffe and Stephenson, 2003). Table 10 shows the TSS values computed for each Z value. Overall, most Z values resulted in negative TSS scores, which imply poor forecast skill. However, the only two Z values that resulted in positive TSS scores, were the 41 and 41.5 dBZ thresholds. These Z thresholds correspond to the same Z value for the minimum rate of FAs. Figure 30 shows the TSS score on a scatter plot against increasing Z values, with a power curve best fit.
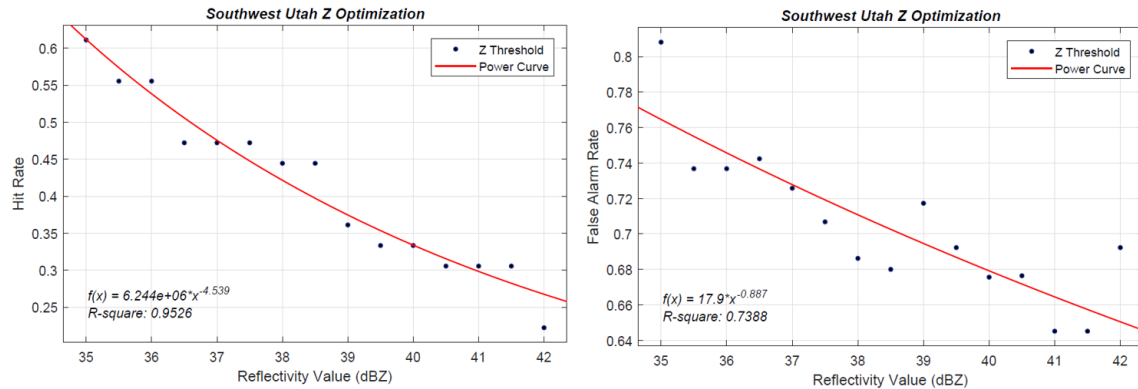
Figure 29. An optimization of Z for the southwest Utah final dataset utilizing the number of hits, misses, CRs, and FAs from the histograms in Figure 28. The red line indicates the power law function for best fit. The hit rate plot mirrors a negative exponential decay with with increasing Z values, while FA rate is more linear. Images produced in MATLAB.
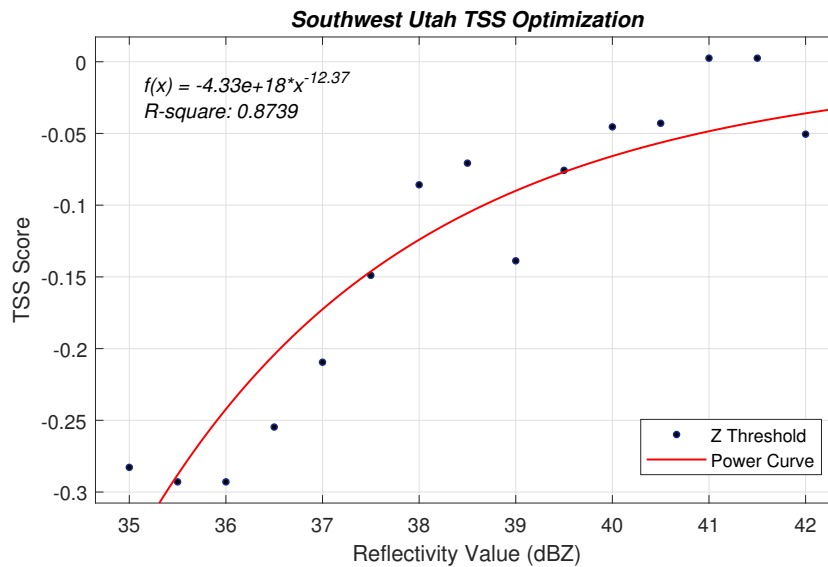
Figure 30. An optimization of Z for the southwest Utah final dataset utilizing the number of hits, misses, CRs, and FAs from the histograms in Figure 28. The red line indicates the power law function for best fit. A positive TSS is observed at 41 dBZ, due to the large decrease in the number of FAs. Image produced in MATLAB.

4.5.2 Differential Reflectivity

While the mean Utah Z varied little between lightning producing cells and non-lightning producing cells, there was a significant difference with Z_{DR}. Table 11 details the mean highest Z_{DR} in non-lightning producing cells and the mean instantaneous Z_{DR} in lightning producing cells. The ≈ 2 dB difference confirms the association of Utah lightning with high Z_{DR} values. This results from the collisions and coalescence of graupel, ice, and water droplets within the mixed phase of thunderstorms. This process then causes hydrometeors to grow, allowing for increased detection by Z_{DR}.

Similar to Z, an optimization of Z_{DR} for the Utah dataset was accomplished using histogram data in Figure 31. The hit rate, FA rate, and TSS were then computed for varying Z_{DR} thresholds. Table 12 shows the three forecast metrics computed for 13 different Z_{DR} thresholds. A perfect hit rate of 1.0000 was recorded for 1.25 dB and 1.30 dB, but both thresholds also had the highest FA rates. Like the Z optimization, lower Z_{DR} thresholds resulted in higher hit rates, but increased FA rates. Increasing
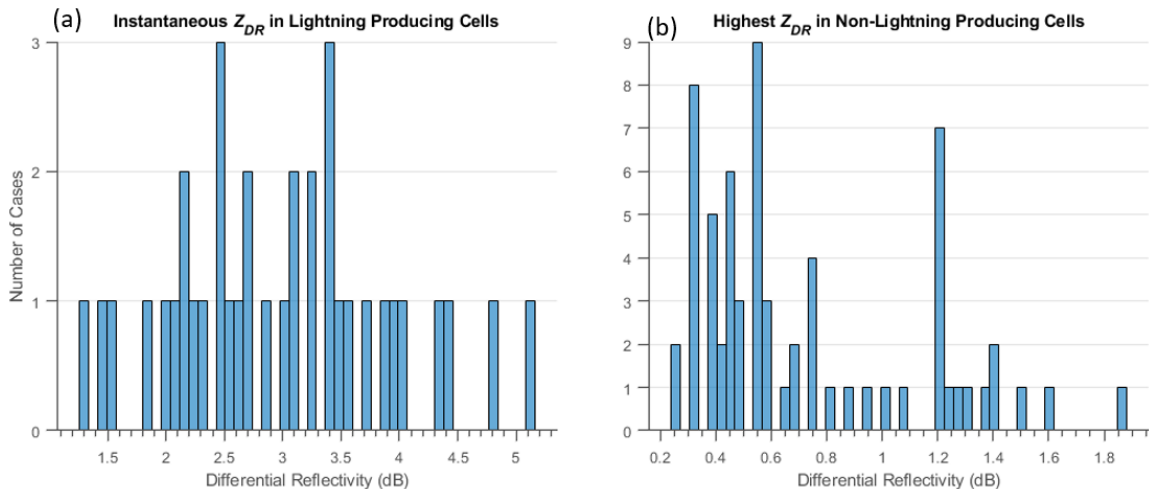
Figure 31. A histogram showing (a) the instantaneous Z_{DR} in lightning producing cells and (b) the highest Z_{DR} in non-lightning producing cells. The overall average Z_{DR} was 1.57 dB, with (a) averaging 2.98 dB and (b) averaging 0.814 dB. Images produced in MATLAB.

66

Mean Southwest Utah Differential Reflectivity

Mean Highest Z_{DR}		Mean Instantaneous Z_{DR}	
Lightning DNE	0.814 dB	Lightning Occurs	2.98 dB

Table 11. The mean highest Z_{DR} recorded in non-lightning producing cells and the mean instantaneous Z_{DR} in lightning producing cells. The highest Z_{DR} value was defined as the highest recorded dB value for a non-lightning producing cell. Conversely, the instantaneous Z_{DR} was the differential reflectivity value at the time of lightning initiation.

Southwest Utah Z_{DR} Performance

Z_{DR} Value (dB)	Hit Rate	FA Rate	TSS
1.25	1.0000	0.2000	0.8636
1.30	1.0000	0.1818	0.8787
1.35	0.9722	0.1666	0.8661
1.40	0.9722	0.0789	0.9267
1.45	0.9444	0.0810	0.8989
1.50	0.9444	0.0810	0.8989
1.55	0.9166	0.0571	0.8863
1.60	0.9166	0.0571	0.8863
1.65	0.9166	0.0294	0.9015
1.70	0.9166	0.0294	0.9015
1.75	0.9166	0.0294	0.9015
1.80	0.9166	0.0294	0.9015
1.85	0.8888	0.0300	0.8737

Table 12. A tabular summary indicating the hit rate, FA rate, and TSS for different Z_{DR} thresholds. Note: The hit rate and FA rate are not the same as POD and FAR, respectively. They are values obtained from counting the number of hits, misses, CRs, and misses using histogram data obtained from Figure 31.

the Z_{DR} threshold decreased the FA rate, but at the expense of hit rate. Figure 32 shows the hit/FA rate values from Table 12 plotted with a best fitting power curve. Both scatter plots show the inverse relationship between the two forecast metrics, as made evident by the decline in forecast performance with increasing Z_{DR} thresholds.

A better indicator of overall forecast skill for Z_{DR} over hit rate and FA rate alone is TSS. Figure 33 shows the TSS data from Table 12 plotted against increasing Z_{DR} values, with a best fitting power curve. The leveling of the power curve at ≈ 1.50 dB corresponded with the highest hit rates and lowest FA rates. Unlike the Z TSS optimization, all TSS scores for Z_{DR} were positive, which suggest relatively high forecast skill in the chosen DP thresholds. This was because Travis' Z_{DR} threshold was too easily met, regardless whether the cell produced lightning or not. The large difference in the optimal Z_{DR} values for Utah and CCAFS/KSC lightning initiation indicate that Z_{DR} lightning prediction is not geographically robust. This unanticipated result may suggest that other DP radar variables follow similar spatial tendencies as Z_{DR}.
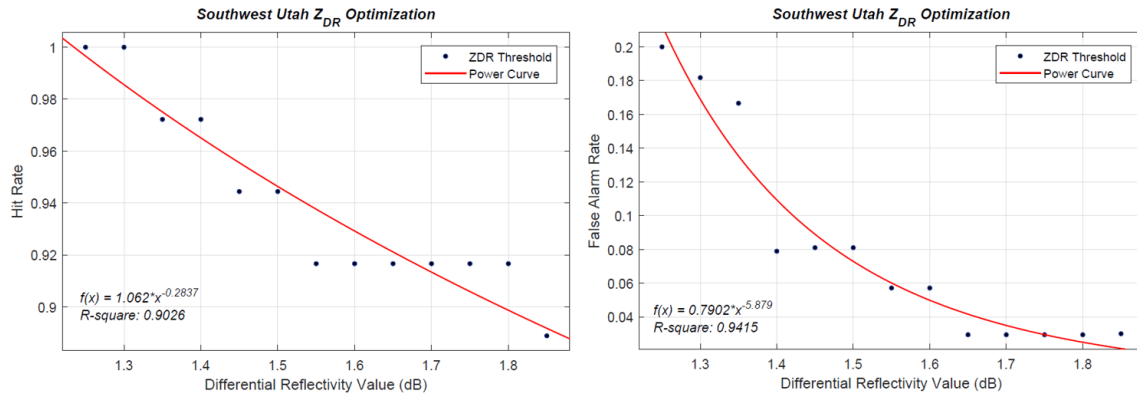
Figure 32. An optimization of Z_{DR} for the southwest Utah final dataset utilizing the number of hits, misses, CRs, and FAs from the histograms in Figure 31. The red line indicates the power curve best fit. Hit rate appears to decrease more linearly than FA rate, which decreases similar to a negative exponential. Images produced in MATLAB.
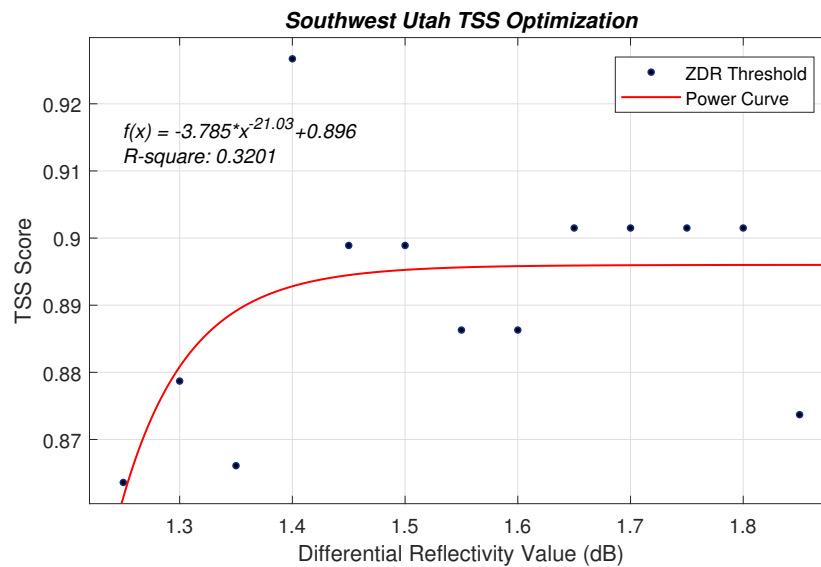
Figure 33. An optimization of Z_{DR} for the southwest Utah final dataset utilizing the number of hits, misses, CRs, and FAs from the histograms in Figure 31. The red line indicates the power curve best fit. Flattening of the curve around 1.50 dB suggests that Z_{DR} values any higher result in similar scores. Image produced in MATLAB.

69

V. Conclusions

Chapter V summarizes the results of this study and provides insight and reasoning behind each outcome. This chapter also explains the additional research that should be conducted in order to fill knowledge gaps, streamline future lightning-related research, and improve upon the findings of this study.

5.1 Summary

Lightning is a dangerous weather phenomenon that causes significant impacts to life and property. Many USAF air and space operations require accurate thunderstorm forecasts so that safety precautions are taken in order to minimize lightning impacts. The 45 WS is entrusted with mitigating thunderstorm impacts for America's manned spaceflight port, over 25,000 personnel, and more than \$20 billion in assets at CCAFS/KSC and Patrick AFB (Roeder, 2018). Weather radar is the primary meteorological tool utilized by 45 WS forecasters for short-term lightning prediction. Improving upon pre-existing lightning prediction methods, such as the Gremillion and Travis methods, can bolster personnel safety and lightning forecast accuracy. Additionally, if the two prediction methods verified well in Utah, it could suggest that radar lightning signatures are identical across different climates and potentially be used in the creation of a new lightning product within the NEXRAD network.

A prior study by Gremillion and Orville (1999) showed that $Z \geq 40$ dBZ at the $-10°C$ thermal height, for two consecutive volume scans, was the best predictor for CG lightning initiation in the CCAFS/KSC area. However, with the advent of DP radar into the NEXRAD network the early 2010s, research studies regarding forecast skill using DP radar began to populate. Woodard et al. (2012) and Thurmond (2014) were two DP studies that suggested a combination of Z and Z_{DR} predictors

70

can improve forecast skill over methods utilizing Z alone. This was verified by a follow-up study conducted by Travis (2015). Travis found that the $Z \geq 36.5$ dBZ with $Z_{DR} \geq 0.31$ dB at the $-10°C$ thermal height was the best combination of radar parameters for lightning prediction in the CCAFS/KSC area. Travis indicated that Z_{DR} was the preferred DP predictor, due to elevated Z_{DR} values indicating the presence of wet ice particles and supercooled water droplets in Florida-based thunderstorms. These two mixed phase hydrometeors are the primary components in the cloud electrification process and generate a Z_{DR} column that can be easily detected by weather radar.

Gremillion and Orville (1999) utilized both the local WSR-88D and the NLDN for their research. Travis (2015), however, used the same WSR-88D and the 4DLSS at CCAFS/KSC. This study utilized an identical lightning detection system to Travis, the TA LMA, and KICX and KMTX WSR-88Ds. One objective of this study was to research the applicability of both lightning prediction methods to a new geographical area. This was accomplished by applying both methods to 102 isolated, warm-season thunderstorms spanning three years across southwest Utah. By testing the traditional radar method from Gremillion and Orville (1999), it allowed the opportunity to compare forecast skill between non-DP and DP techniques. Lastly, the results of this study were also compared to Olsen (2018), where she completed a similar experiment. Olsen applied Travis' thresholds to the Washington, D.C. area to test the usability of the CCAFS/KSC radar parameters in a new climate. Olsen's results revealed that the forecast metrics between that study and Travis' were statistically different and that Travis' thresholds did not perform well for the new area. By comparing the results of this study to Olsen's, it allowed for the comparison of DP prediction thresholds across different climates, and to infer new spatial information about DP lightning prediction.

71

5.1.1 Travis Lightning Prediction Method

The first results from this study concluded that the lightning initiation methods from Travis (2015) do not perform well when applied to the southwest Utah area. This was made evident by multiple tables and figures, which document the poor performance of his DP method. Figure 19 shows the significant difference of the five forecast metrics between the southwest Utah and CCAFS/KSC areas. The only metric that was statistically similar was POD, where a slight overlap in the 95% CI bounds was observed. This suggests that POD for this study was comparable to Travis (2015). Interestingly, this was an identical finding to Olsen (2018), where it was found that POD was similar for the Washington, D.C. and CCAFS/KSC areas.

The poor performance of Travis' method to Utah is further verified by the comparison of the three OUIs. Figure 20 shows the three modified OUIs among southwest Utah and CCAFS/KSC. All three OUIs were statistically different from one another, indicating the sub-par performance of Travis' thresholds in Utah. However, OUI† and OUI shared the highest scores for both areas, suggesting that either limiting the 'MaxLeadTime' term to 30 min or using 30 min alone are equal. The reason for the significant difference between the CCAFS/KSC and Utah OUIs was the high number of FAs for the Utah dataset, which comprised 55% of the total forecast outcomes. While the forecast metrics were almost entirely different from one another, lead times were comparable. It was also interesting to note that Utah's OUIs varied little among each other, which concurred with an OUI comparison study completed in Nava (2018). Figure 21 shows the mean and median lead times for the two locations. A large amount of overlap by the CI bounds indicated that they were statistically similar. This finding was identical to Olsen (2018), where it was concluded there was no significant difference between the Washington, D.C. and CCAFS/KSC lead times.

72

Comparing the results from Olsen (2018) and Utah reveal new findings. Figure 22 shows that POD, FAR, and CSI are statistically similar, while PFA and TSS were different. It was interesting that despite the significant differences in climate and terrain between Washington, D.C. and Utah, the forecast metrics remain generally alike. Similarities were further supported by the comparison of the three OUIs. Figure 23 shows that the three OUIs are similar, with OUI being the highest performing metric for both locations. Lead times between the two locations were also compared in order to document similarities/differences. Table 6 shows that both locations coincidentally had the same maximum lead time. Similar to the Travis comparison, lead times were statistically similar, despite different geographical regions. As both of these locations are along the same latitude, it is possible to suggest that additional locations along the same latitude (i.e. Kansas City, Cincinnati) have similar LISTs. This is especially true for mid-latitude locations, where frontal systems dominate the weather pattern.

5.1.2 Gremillion Lightning Prediction Method

The highest performing LIST forecast method from Gremillion and Orville (1999) does not perform well when applied to the southwest Utah area. Similar to the previous locations, various figures and tables indicate poor performance. Figure 25 shows the five forecast metrics for Gremillion's method applied to the Utah dataset, compared to Travis' method for the other two locations. PFA and CSI were similar for Washington, D.C. and southwest Utah despite different forecast methodologies. Further evidence of performance was observed in the OUI comparisons. Figure 26 indicate that using Gremillion's method for Utah is inferior to Travis' method for the other two locations. OUI was the highest scoring metric for all three locations. Lead times were also compared to one another. Despite requiring stricter radar criteria (one additional volume scan than Travis and higher Z), the median lead time was

73

higher for Utah than CCAFS/KSC. This may be the result of thunderstorm intensity differences. Figure 27 shows the lead times with 95% CI bounds. Lead times were also all similar, as made evident by the overlapping CI bounds in all three comparisons.

5.1.3 Poor Forecast Performance Rationale

Reasons for the poor performance of both the Gremillion and Travis lightning prediction methods stem from the terrain and cloud droplet differences between Utah and central Florida. Utah elevation averages 2,300 ft, while CCAFS/KSC is approximately at sea level. Altitude already has a documented and well-known effect on electrical fields, and therefore, lightning discharges. Utah summers are also composed of a continental hot dry atmosphere, while Florida summers are in a maritime warm moist atmosphere. Cloud droplet spectra differences between the two locations are also well known. Continental cumulus clouds have a high concentration of small droplets and narrow size spectrum, while maritime cumulus clouds have a small concentration of large droplets and a broad size spectrum (Rogers and Yau, 1989). These droplet differences have an impact on the thunderstorm charging mechanisms, and thus, an effect on lightning initiation. This was further proven in the differences between optimal Z_{DR} values in Utah and CCAFS/KSC. Travis found the optimal Z_{DR} value to be ≥ 0.31 dB. For Utah, Z_{DR} needs to be at least 1.40 dB or greater, depending on the desired balance of hits to FAs. This suggests that Z_{DR} lightning initiation is not geographically robust, as opposed to Z which performs well for any location around 35 dBZ at the $-10°$C thermal height (Yang and King, 2010).

Significant climate differences between southwest Utah, CCAFS/KSC, and Washington, D.C. are likely why both prediction methods performed poorly. The summer weather in Utah is primarily determined by the onset, location, and intensity of heat lows that formed as a result of the North American Monsoon. This seasonal fea-

74

ture brings widespread thunderstorms and precipitation across the southwest United States. This is a drastic difference to the climate of CCAFS/KSC, where land and sea-breeze interactions are the primary weather driver. These micro-scale meteorological features are difficult to predict, as the onset and timing is controlled by many local factors. Washington, D.C. is more similar to CCAFS/KSC than Utah, because of the similar east coast locations. However, weather in Washington, D.C. is primarily driven by synoptic-scale mid-latitude weather features such as cold and warm fronts. Utah also experiences similar mid-latitude fronts, but the topography and monsoon is accepted as the primary weather driver.

It appeared during the course of the research that Travis' lightning prediction method was better than Gremillion's for Utah. However, Travis' Z_{DR} threshold was met in every case, rendering it useless as a predictor of lightning. Also, Travis' method only required one volume scan, giving his method more lead time than Gremillion's. Instead, it was Travis' lower Z threshold that caused his method to perform better than Gremillion's. Similar to conclusions in Olsen (2018), simplicity is better when forecasting operationally. Therefore, utilizing Z alone for predicting Utah lightning is superior over a mix of radar variables, and should be used as the determining factor.

5.1.4 Southwest Utah Z and Z_{DR} Optimization

If Z is found to be the determining factor for a particular location, weather forecast units should tailor this radar threshold across their respective AORs. Accomplishing a generalized optimization for the southwest Utah area revealed that the hits and FAs are inversely related. Forecasters need to remain wary of choosing a Z value that results in the highest POD, because it can also have a large FAR/PFA. FAs need to be regarded just as highly as hits due to the impact on forecaster credibility. If a unit's FAR/PFA is consistently too high, customers will disregard forecast warnings

75

and not take the necessary safety precautions ultimately putting them at risk. While fully optimizing the Utah dataset extends beyond the scope of this study, Table 10 shows the impacts of hit rate, FA rate, and TSS across different Z values for Utah.

Lastly, as an additional measure in this study, the mean highest and instantaneous Z_{DR} was optimized. Table 12 shows the hit rate, FA rate, and TSS score across different Z_{DR} thresholds. Utilizing the 0.31 dB threshold from Travis (2015) was too low for the Utah region, because it caused too many FAs. Raising the DP requirement to a value of at least 1.25 dB or greater would result in better performance. This was supported by the TSS optimization, indicating 1.45 or 1.80 dB as preferred Z_{DR} thresholds. This also indicated that Z_{DR} thresholds vary greatly by region and would require complete optimization in order to use them confidently in forecasts. As such, Z is found to be the determining factor for Utah lightning initiation. Optimizing this value for AORs will produce better results than a fixed combination of Z and Z_{DR}.

5.2 Recommendations for Future Work

This study provided new insight into the challenging problem of forecasting lightning initiation, however, continued research on this subject should be considered in order to further improve forecast techniques. More specifically, completing regional optimizations of weather radar lightning initiation signatures across the nation. Conducting an optimization for each of the 159 WSR-88Ds in the NEXRAD network is the ideal solution as it could warn weather forecasters of an impending lightning strike. This would greatly increase personnel safety and minimize lightning's costly impacts. However, manually optimizing radar lightning initiation thresholds for several hundred different locations would be a tremendous task and needs to be computerized. One such automation process, known as machine learning, offers a potential solution.

5.2.1 Optimize and Refine Current Systems

Machine learning, also regarded as artificial intelligence (AI) methods, should be utilized to conduct optimizations across each region, as it has been proven in this study and Olsen (2018) that lightning initiation signatures are not universal. It is likely that across different regions there exists different and higher-performing lightning determining factors than Z. For instance, this study and Olsen (2018) agree that Z is the determining factor, while others (Woodard et al. (2012), Thurmond (2014), Travis (2015)) suggest the use of Z_{DR}. Use of Level III radar products, such as the Hydrometeor Classification Algorithm or Echo Tops, could potentially be used to predict lightning in other areas. These optimizations could be accomplished using radar data against other LMAs (i.e. Alabama, Colorado), the NLDN, or the Geostationary Operational Environmental Satellite (GOES)-16 Satellite Geostationary Lightning Mapper (GLM). Bottou et al. (2018) offers a potential starting point for mathematical optimization options relating to large-scale machine learning methods.

5.2.2 Use Total Lightning Methods

In addition to machine learning/AI methods, it would be worthwhile to test Travis' lightning prediction method against another prediction method that includes total lightning (IC/CC/CG). Gremillion's method was designed for use in forecasting CG lightning strikes. Utilizing another total lightning method may produce unanticipated research results. One potential total lightning initiation/cessation forecast method developed for the 45 WS is detailed in Roeder and Pinder (1998). A list of empirical forecast rules is described here which contains the 'Pinder Principles' for lightning cessation and six different lightning onset scenarios using weather radar. Testing this Florida prediction method in new geographical regions may reveal new findings.

5.2.3 Develop Procedures Similar to LLWAS

The future of lightning forecasts will likely be as effective as the prediction of wind shear events generated by microbursts at major airports across the United States. The FAA attributes wind shear as the probable cause for over 35 air carrier and air transport accidents between 1964 and 1976 (FAA, 1983). Once a seemingly impossible weather event to forecast, wind shear events have largely been mitigated by the invention of a radar-based prediction system. The Low Level Wind Shear Alert System (LLWAS) utilizes a network of ground-based sensors and weather radars to alert pilots and air traffic controllers of impending wind shear events (Vaisala, 2018a).

In a similar way, ground or space-based sensors could be utilized with weather radar to support air and space launch operations at USAF facilities by prompting weather forecasters of an imminent lightning threat. Such a system would reduce thunderstorm disruptions, such as the 15 min delay for lightning threats, to USAF air and space operations and increase overall operational effectiveness and safety. The key to developing such a system is possible through the use of machine learning and AI methods to develop region-specific radar lightning initiation signatures. The results of this study suggest that lightning safety in USAF air and space operations could greatly be improved upon if machine learning and AI optimization techniques are employed onto current and future weather radar and lightning detection technology.

														Travis Method			Gremillion Method				
Case	Date	Start Time	End Time	LatS	LatN	LonE	LonW	Radar	Avg -10C (ft)	Correction	Actual Initiation	ZDR Initiation	Z Initiation	Both Met	Result	LT (min)	Both Met	Result	LT (min)	Z (dBZ)	ZDR (dB)
1	8/8/2015	1800Z	1900Z	38.167	38.408	-113.384	-113.7		16122	10118	18 hours, 7 mins, 33.6 secs	17:56:48	18:00:33	18:00:33	Hit	7	18:04:18	Hit	3	43	3.12
2	8/11/2015	1800Z	1830Z	38.338	38.794	-112.341	-112.649		16566	10562	18 hours, 2 mins, 28.8 secs	17:30:56	17:40:30	17:40:30	Hit	22	17:45:33	Hit	17	41	2.84
3	8/13/2015	2110Z	2200Z	38.519	38.953	-112.248	-112.605		17893	11889	21 hours, 10 mins, 33.5 secs	20:50:15	20:53:57	20:53:57	Hit	17	21:03:25	Hit	7	37	3.4
4	8/21/2015	2030Z	2130Z	38.651	38.887	-112.759	-113.056		16131	10127	20 hours, 34 mins, 45.4 secs	20:26:16	20:30:04	20:30:04	Hit	5	20:41:07	Miss		42	3.88
5	8/22/2015	2120Z	2200Z	38.425	38.563	-113.748	-113.913		16378	10374	21 hours, 28 mins, 58.9 secs	21:02:13	21:22:08	21:22:08	Hit	6	21:32:04	Miss		40	2.72
6	8/23/2015	2100Z	2130Z	38.316	38.486	-113.55	-113.759		17126	11122	DNE	20:55:23	21:06:51	21:06:51	FA		Never Met	CR		40	1.5
7	8/23/2015	2000Z	2100Z	38.335	38.412	-112.127	-112.309		17126	11122	DNE	19:57:26	20:01:18	20:01:18	FA		20:05:07	FA		40	1.38
8	8/27/2015	2025Z	2100Z	38.335	38.439	-112.556	-112.764		17054	11050	20 hours, 24 mins, 36.9 secs	20:13:14	20:23:08	20:23:08	Hit	1	20:38:01	Miss		38.5	2.5
9	8/27/2015	1950Z	2035Z	40.257	40.444	-112.341	-112.594	KMTX	17054	15962	19 hours, 59 mins, 33.8 secs	19:46:33	19:51:27	19:51:27	Hit	8	19:56:21	Hit	3	43	5.13
10	8/29/2015	2130Z	2215Z	38.556	38.714	-112.094	-112.248		17193	11189	DNE	21:26:18	21:33:57	21:33:57	FA		21:45:25	FA		42	3.31
11	8/29/2015	2300Z	2330Z	39.763	39.966	-112.984	-113.187	KMTX	17193	16101	23 hours, 1 min, 10.5 secs	22:54:10	22:57:51	22:57:51	Hit	4	23:01:30	Miss		50.5	3.56
12	8/30/2015	2230Z	2300Z	39.626	39.862	-112.281	-112.561	KMTX	17604	16512	DNE	22:31:45	22:39:07	22:39:07	FA		22:42:49	FA		44	2.13
13	9/8/2015	0420Z	0545Z	38.428	38.67	-112.523	-113.16		16732	10728	DNE	4:02:10	4:09:48	4:09:48	FA		Never Met	CR		38	1.25
14	9/13/2015	2120Z	2200Z	38.758	38.879	-112.71	-112.885		15962	9958	DNE	21:17:33	21:22:29	21:22:29	FA		21:27:25	FA		40.5	1.31
15	9/15/2015	1820Z	1900Z	38.401	38.604	-112.6	-112.852		15354	9350	DNE	18:27:33	18:31:22	18:31:22	FA		Never Met	CR		36.5	0.38
16	9/23/2015	1940Z	2010Z	38.428	38.483	-112.589	-112.731		14925	8921	19 hours, 45 mins, 58.3 secs	19:36:43	19:40:31	19:40:31	Hit	5	19:49:15	Miss		45	4.06
17	9/23/2015	1940Z	2020Z	38.505	38.62	-113.154	-113.292		14925	8921	DNE	19:44:20	19:49:15	19:49:15	FA		19:59:08	FA		38.5	1.88
18	9/23/2015	2120Z	2200Z	38.829	38.923	-112.863	-112.99		14925	8921	21 hours, 23 mins, 30.5 secs	21:07:43	21:17:32	21:17:32	Hit	6	21:45:43	Miss		33.5	4.81
19	9/23/2015	2040Z	2200Z	39.856	39.999	-112.193	-112.435	KMTX	14925	13833	DNE	20:48:51	20:56:15	20:56:15	FA		Never Met	CR		39	2.94
20	5/15/2016	1910Z	2000Z	40.172	40.303	-112.297	-112.621	KMTX	13979	12887	DNE	Never Met	Never Met	Never Met	CR		Never Met	CR		34.5	2
21	5/16/2016	1600Z	1700Z	40.177	40.38	-112.797	-113.055	KMTX	11974	10882	DNE	Never Met	Never Met	Never Met	CR		Never Met	CR		35	0.81
22	5/16/2016	1840Z	1930Z	40.007	40.177	-112.286	-112.462	KMTX	11974	10882	DNE	18:54:37	19:02:02	19:02:02	FA		Never Met	CR		38	0.38
23	5/17/2016	1730Z	1800Z	39.738	39.886	-112.5	-112.736	KMTX	11407	10315	DNE	17:27:15	17:42:08	17:42:08	FA		Never Met	CR		36.5	0.75
24	5/17/2016	2100Z	2200Z	38.507	38.721	-112.917	-113.099		11407	5403	21 hours, 9 mins, 7.6 secs	20:58:29	21:07:01	21:07:01	Hit	2	21:11:16	Miss		42	2.31
25	5/17/2016	2130Z	2215Z	38.304	38.535	-113.489	-113.615		11407	5403	DNE	21:32:30	21:41:03	21:41:03	FA		Never Met	CR		37	0.31
26	5/24/2016	1850Z	1945Z	38.54	38.859	-112.462	-112.72		11478	5474	18 hours, 51 mins, 54.7 secs	18:39:03	18:49:20	18:49:20	Hit	2	Never Met	Miss		36.5	2.56
27	5/24/2016	2320Z	0000Z	38.496	38.644	-113.022	-113.192		11478	5474	DNE	23:26:22	23:30:01	23:30:01	FA		Never Met	CR		37.5	0.31
28	5/25/2016	1930Z	2000Z	39.628	39.825	-112.775	-113.044	KMTX	11054	9962	DNE	19:30:19	19:38:56	19:38:56	FA		Never Met	CR		37	2
29	5/25/2016	2300Z	0000Z	38.826	38.979	-113.176	-113.324		11054	5050	DNE	23:03:03	23:18:01	23:18:01	FA		23:23:00	FA		46.5	0.5
30	5/26/2016	1950Z	2030Z	38.694	38.842	-112.582	-112.769		11187	5183	DNE	19:49:48	19:54:10	19:54:10	FA		19:58:31	FA		46.5	0.44
31	5/27/2016	1540Z	1630Z	39.831	40.001	-112.357	-112.588	KMTX	11413	10321	DNE	15:38:27	15:42:09	15:42:09	FA		15:49:34	FA		46	0.88
32	5/28/2016	1930Z	2030Z	39.88	40.023	-112.401	-112.593	KMTX	12301	11209	DNE	19:29:59	19:33:43	19:33:43	FA		19:37:26	FA		40.5	1.06
33	5/29/2016	1800Z	1900Z	40.001	40.177	-112.527	-112.731	KMTX	12572	11480	DNE	18:04:48	18:16:00	18:16:00	FA		18:19:45	FA		44	0.75
34	6/30/2016	2100Z	2200Z	39.781	40.001	-112.489	-112.775	KMTX	16694	15602	21 hours, 0 min, 5.6 secs	20:51:47	20:59:09	20:59:09	Hit	1	21:06:32	Miss		39	2.25
35	7/22/2016	2045Z	2200Z	38.672	38.87	-112.714	-112.967		17586	11582	DNE	20:46:07	20:50:02	20:50:02	FA		Never Met	CR		40.5	0.25
36	7/22/2016	2120Z	2230Z	38.436	38.595	-113.055	-113.22		17586	11582	DNE	21:27:05	21:34:27	21:34:27	FA		Never Met	CR		40	0.31
37	7/25/2016	1940Z	2100Z	38.54	38.738	-112.967	-113.154		16821	10817	DNE	19:38:47	19:43:06	19:43:06	FA		19:47:24	FA		43	0.5
38	7/25/2016	1940Z	2100Z	38.348	38.518	-113.214	-113.445		16821	10817	DNE	19:38:47	19:38:47	19:38:47	FA		19:51:41	FA		38.5	0.38
39	7/26/2016	2000Z	2100Z	38.024	38.221	-113.198	-113.379		17572	11568	20 hours, 3 mins, 25.9 secs	19:50:27	19:59:50	19:59:50	Hit	4	20:09:13	Miss		45	1.56
40	7/29/2016	1910Z	2000Z	38.024	38.15	-112.659	-112.841		17000	10996	19 hours, 11 mins, 44.5 secs	19:05:11	19:10:02	19:10:02	Hit	2	19:19:43	Miss		36.5	1.44
41	7/30/2016	1845Z	2000Z	38.469	38.666	-112.89	-113.06		17062	11058	DNE	18:49:15	18:56:23	18:56:23	FA		19:01:01	FA		45.5	0.31
42	7/30/2016	1945Z	2100Z	38.298	38.447	-113.538	-113.687		17062	11058	DNE	19:44:35	19:49:25	19:49:25	FA		19:59:05	FA		51	0.57
43	7/30/2016	2010Z	2100Z	38.465	38.65	-113.137	-113.357		17062	11058	20 hours, 18 mins, 50.6 secs	20:18:27	Never Met	Never Met	Miss		20:37:52	Miss		35	2
44	8/1/2016	1940Z	2030Z	38.227	38.414	-113.445	-113.626		17268	11264	19 hours, 44 mins, 42.6 secs	19:36:50	Never Met	Never Met	Miss		20:24:08	Miss		21.5	3.06
45	8/2/2016	1900Z	2000Z	38.266	38.453	-113.48	-113.667		17502	11498	19 hours, 46 mins, 27.9 secs	19:01:28	19:14:52	19:14:52	Hit	32	19:18:35	Hit	26	50	4.44
46	8/3/2016	1850Z	1930Z	38.404	38.574	-113.063	-113.233		17474	11470	18 hours, 55 mins, 10.7 secs	18:47:27	18:37:54	18:37:54	Hit	18	19:06:33	Miss		29	3.75
47	8/5/2016	1730Z	1810Z	38.343	38.541	-113.617	-113.821		17737	11733	DNE	17:26:58	17:34:24	17:34:24	FA		17:38:08	FA		44.5	1.75
48	8/5/2016	2210Z	2300Z	38.393	38.568	-112.898	-113.162		17737	11733	DNE	22:07:00	22:14:22	22:14:22	FA		22:18:04	FA		48.5	0.44
49	8/18/2016	2110Z	2200Z	38.645	38.843	-112.761	-112.931		15603	9599	21 hours, 12 mins, 8.1 secs	21:08:32	21:23:13	21:23:13	Miss		21:28:06	Miss		21.5	2.69
50	8/22/2016	2235Z	2315Z	38.305	38.48	-113.178	-113.37		15523	9519	22 hours, 31 mins, 34.3 secs	22:03:55	22:18:39	22:18:39	Hit	13	22:23:33	Hit	8	39	3.94
51	8/26/2016	1900Z	1945Z	38.354	38.497	-113.156	-113.365		14398	8394	DNE	18:49:11	19:18:36	19:18:36	FA		19:23:16	FA		36.5	0.25
52	9/11/2016	2130Z	2200Z	38.629	38.837	-112.887	-113.063		15911	9907	DNE	Never Met	21:46:36	Never Met	CR		21:50:28	FA		40.5	0.94
53	9/30/2016	1950Z	2020Z	38.283	38.502	-112.563	-112.832		15037	9033	DNE	19:47:45	Never Met	Never Met	CR		Never Met	CR		36	0.38
54	5/8/2017	1900Z	2010Z	39.771	39.991	-112.508	-112.728	KMTX	11689	10597	DNE	19:16:52	19:28:02	19:28:02	FA		19:31:57	FA		42	0.56
55	5/9/2017	1900Z	2000Z	39.639	39.837	-112.365	-112.557	KMTX	12546	11454	DNE	18:58:14	19:03:07	19:03:07	FA		19:26:28	FA		41	0.75
56	7/9/2017	2100Z	2145Z	38.338	38.524	-113.041	-113.189		17037	11033	21 hours, 8 mins, 56.0 secs	20:59:20	21:03:05	21:03:05	Hit	6	21:06:52	Hit	2	47	4.38
57	7/12/2017	2020Z	2100Z	38.447	38.579	-113.134	-113.332		17326	11322	20 hours, 20 mins, 30.0 secs	20:09:42	20:14:50	20:14:50	Hit	7	20:19:59	Hit	1	51.5	3
58	7/12/2017	2115Z	2200Z	38.393	38.563	-113.458	-113.623		17326	11322	DNE	21:06:17	21:16:34	21:16:34	FA		Never Met	CR		39	0.69
59	7/18/2017	1915Z	2030Z	38.371	38.541	-113.189	-113.381		17929	11925	DNE	19:23:32	19:29:01	19:29:01	FA		19:40:01	FA		50.5	0.69
60	7/21/2017	2200Z	2245Z	38.255	38.398	-113.134	-113.266		17659	11655	DNE	22:12:43	22:17:37	22:17:37	FA		22:22:31	FA		44	0.31
61	7/22/2017	2330Z	0000Z	38.574	38.761	-113.354	-113.557		18015	12011	23 hours, 36 mins, 32.5 secs	22:38:46	22:38:35	22:38:35	FA		23:43:29	Miss		42	2.19
62	7/23/2017	2045Z	2130Z	38.64	38.87	-112.766	-112.98		17487	11483	DNE	20:50:53	20:55:47	20:55:47	FA		Never Met	CR		37	0.31
63	7/25/2017	2110Z	2200Z	39.832	40.002	-112.239	-112.464	KMTX	18105	17013	DNE	21:34:33	Never Met	Never Met	CR		Never Met	CR		29	0.57
64	7/25/2017	2130Z	2200Z	38.162	38.31	-113.37	-113.546		18105	12101	DNE	21:40:30	21:55:34	21:55:34	FA		21:55:34	FA		46.5	0.56
65	7/29/2017	2300Z	0000Z	38.398	38.607	-113.079	-113.315		17775	11271	23 hours, 1 min, 46.0 secs	23:01:22	23:11:09	23:11:09	Miss		23:16:01	Miss		27	2.5
66	7/31/2017	2200Z	2300Z	38.2	38.398	-112.607	-112.711		16848	10844	DNE	22:15:03	22:28:50	22:28:50	FA		22:32:48	FA		42.5	1.2
67	8/1/2017	1815Z	2000Z	38.305	38.464	-112.629	-112.799		16747	10743	DNE	18:11:26	18:16:20	18:16:20	FA		Never Met	CR		37	0.44
68	8/1/2017	1900Z	2000Z	38.327	38.469	-112.513	-112.667		16747	10743	DNE	19:02:17	19:06:56	19:06:56	FA		19:16:16	FA		43	0.56
69	8/2/2017	1830Z	1900Z	38.321	38.453	-112.684	-112.826		17101	11097	DNE	18:33:26	18:43:13	18:43:13	FA		18:48:07	FA		40	0.31
70	8/2/2017	1900Z	1935Z	38.42	38.513	-112.612	-112.782		17101	11097	DNE	18:59:52	19:04:46	19:04:46	FA		19:29:15	FA		37.5	0.38
71	8/2/2017	2000Z	2030Z	38.299	38.415	-113.035	-113.183		17101	11097	DNE	20:03:33	20:08:26	20:08:26	FA		20:18:01	FA		41	0.57
72	8/3/2017	1930Z	2000Z	38.398	38.541	-113.135	-113.277		16847	10843	19 hours, 30 mins, 54.0 secs	19:09:40	19:09:40	19:09:40	Hit	21	19:43:06	Miss		28	3.88
73	8/3/2017	1950Z	2030Z	38.349	38.497	-112.601	-112.761		16847	10843	19 hours, 56 mins, 11.7 secs	19:19:28	19:19:28	19:19:28	Hit	37	19:29:15	Miss		32	2.06
74	8/5/2017	2140Z	2220Z	38.393	38.618	-113.13	-113.288		17349	11345	21 hours, 40 mins, 36.7 secs	21:36:35	21:41:28	21:41:28	Miss		21:46:08	Miss		35	3.5
75	8/6/2017	2100Z	2130Z	38.349	38.519	-113.194	-113.409		17026	11022	DNE	20:52:51	21:02:38	21:02:38	FA		21:07:32	FA		42.5	0.44
76	8/7/2017	1830Z	1900Z	39.898	40.062	-112.585	-112.75	KMTX	16166	15074	DNE	18:32:05	18:53:26	18:53:26	FA		Never Met	CR		30	0.56
77	8/7/2017	2240Z	2310Z	39.903	40.051	-112.772	-112.909	KMTX	16166	15074	DNE	22:41:24	22:45:50	22:45:50	FA		23:07:55	FA		38.5	0.41
78	8/11/2017	1910Z	1940Z	38.535	38.771	-112.936	-113.134		16023	10019	DNE	19:10:28	19:15:22	19:15:22	FA		19:20:15	FA		43	0.75
79	8/12/2017	1805Z	1835Z	38.512	38.706	-112.969	-113.178		16219	10215	DNE	18:03:46	18:13:33	18:13:33	FA		18:18:27	FA		40	0.75
80	8/12/2017	1805Z	1840Z	38.332	38.502	-113.26	-113.491		16219	10215	DNE	18:23:21	18:28:14	18:28:14	FA		Never Met	CR		36.5	0.66
81	8/16/2017	2120Z	2310Z	39.859	40.035	-112.272	-112.508	KMTX	15476	14384	DNE	21:14:18	21:20:07	20:20:07	Hit	4	Never Met	Miss		27	1.2
82	8/21/2017	2020Z	2050Z	39.722	39.892	-112.744	-112.931	KMTX	16379	15287	DNE	20:38:15	21:21:45	21:21:45	FA		21:25:28	FA		26	1
83	8/21/2017	2020Z	2050Z	40.172	40.444	-112.321	-112.546	KMTX	16000	14908	DNE	19:44:36	Never Met	Never Met	CR		Never Met	CR		31.5	0.5
84	8/22/2017	2020Z	2050Z	38.283	38.48	-112.755	-112.92		15961	9957	20 hours, 23 mins, 59.7 secs	20:11:13	20:20:07	20:20:07	Hit	4	Never Met	Miss		32.5	1.81
85	8/22/2017	2320Z	2350Z	38.299	38.442	-112.975	-113.173		15961	9957	23 hours, 23 mins, 45.7 secs	23:05:05	23:27:38	23:27:38	Miss		23:38:57	Miss		33	1.8
86	8/31/2017	1950Z	2040Z	39.98	40.145	-112.321	-112.546	KMTX	16499	15407	20 hours, 0 min, 34.6 secs	20:13:07	Never Met	Never Met	Miss		Never Met	CR		25	0.56
87	9/6/2017	2000Z	2035Z	38.376	38.486	-112.651	-112.826		16743	10739	20 hours, 0 min, 34.6 secs	19:58:03	20:02:58	20:02:58	Hit	2	20:12:49	Miss		26	0.56
88	9/7/2017	2250Z	2320Z	39.766	39.942	-112.755	-112.964	KMTX	16384	15292	22 hours, 52 mins, 8.4 secs	22:52:16	23:04:18	23:04:18	Miss		23:08:19	Miss		37	3.25
89	5/1/2018	1900Z	1930Z	38.227	38.422	-113.184	-113.335		13253	7249	DNE	19:10:58	Never Met	Never Met	CR		Never Met	CR		36	0.44
90	5/2/2018	1800Z	1830Z	38.463	38.633	-113.052	-113.233		13038	7034	DNE	18:19:55	Never Met	Never Met	CR		Never Met	CR		36	1.2
91	5/14/2018	1900Z	1945Z	38.348	38.584	-113.049	-113.236		15320	9316	DNE	17:58:07	19:27:12	19:27:12	FA		18:21:53	FA		55.5	0.56
92	5/19/2018	1800Z	1900Z	38.265	38.496	-112.646	-112.898		16738	10734	DNE	17:58:07	18:02:46	18:02:46	FA		Never Met	CR		36.5	0.56
93	5/22/2018	1845Z	1915Z	38.188	38.386	-112.783	-113.008		16285	10281	DNE	18:42:01	18:53:19	18:53:19	FA		Never Met	CR		36.5	1.21
94	5/27/2018	1800Z	1845Z	38.255	38.557	-113.102	-113.343		16471	10467	DNE	18:07:22	18:07:22	18:07:22	FA		Never Met	CR		36.5	0.31
95	5/27/2018	2000Z	2030Z	38.227	38.381	-113.178	-113.332		16471	10467	DNE	18:49:31	19:09:06	19:09:06	FA		Never Met	CR		36	0.55
96	5/28/2018	1745Z	1820Z	39.397	39.617	-112.948	-113.145	KMTX	16629	15537	17 hours, 45 mins, 4.5 secs	17:42:21	17:49:49	17:49:49	Miss		Never Met	Miss		31	2.13
97	7/9/2018	2125Z	2150Z	38.287	38.441	-113.189	-113.354		21691	15687	21 hours, 29 mins, 10.7 secs	21:27:03	21:33:12	21:33:12	Miss		21:38:55	Miss		36	3.25
98	7/9/2018	2130Z	2150Z	38.628	38.815	-112.69	-112.876		21691	15687	21 hours, 29 mins, 58.8 secs	21:27:03	21:44:13	21:44:13	Miss		21:57:10	Miss		36.5	1.31
99	7/13/2018	2010Z	2040Z	39.716	39.886	-112.799	-112.97	KMTX	22049	20957	DNE	20:26:21	20:33:49	20:33:49	FA		Never Met	CR		39.5	0.56
100	7/14/2018	2040Z	2115Z	38.199	38.364	-113.134	-113.316		22118	16114	DNE	20:38:37	20:50:07	20:50:07	FA		Never Met	CR		37.5	0.41
101	7/17/2018	1855Z	1930Z	38.452	38.573	-112.876	-113.151		21861	15857	DNE	19:08:09	19:18:54	19:18:54	FA		Never Met	CR		37	1.2
102	7/17/2018	1940Z	2020Z	38.392	38.507	-112.97	-113.2		21861	15857	19 hours, 39 mins, 46.1 secs	19:35:00	19:45:44	19:45:44	Miss		19:56:29	Miss		32	2.63

Bibliography

45 SW (2017). 45th Space Wing Priorities & Commitments 2017. Technical report, USAF, Patrick AFB, Florida, USA.

Avila, E. E., Pereyra, R. G., Aguirre Varela, G. G., and Caranti, G. M. (1999). The Effect of the Cloud-Droplet Spectrum on Electrical-Charge Transfer During Individual Ice-Ice Collisions. *Quarterly Journal of the Royal Meteorological Society*, **125**(557):1669–1679.

Bottou, L., Curtis, F. E., and Nocedal, J. (2018). Optimization Methods for Large-Scale Machine Learning. *SIAM Review*, **60**(2):223–311.

Cooper, M. A. (1995). Emergent Care for Lightning and Electrical Injuries. *Seminars in Neurology*, **15**(3):268–278.

Emersic, C. (2006). *Investigations Into Thunderstorm Electrification Processes*. PhD thesis, The University of Manchester, UK.

FAA (1983). Advisory Circular 120-41: Criteria for Operational Approval of Airborne Wind Shear Altering and Flight Guidance Systems. Technical report, Department of Transportation, Washington, D.C., USA.

Gibson Ridge Software (2018). GR2Analyst Version 2. URL `https://www.grlevelx.com/gr2analyst_2/`.

Gremillion, M. S. and Orville, R. E. (1999). Thunderstorm Characteristics of Cloud-to-Ground Lightning at the Kennedy Space Center, Florida: A Study of Lightning Initiation Signatures as Indicated by the WSR-88D. *Weather and Forecasting*, **14**(5):640–649.

Henderson, A. R. (2005). The bootstrap: A technique for data-driven statistics. Using computer-intensive analyses to explore experimental data. *Clinica Chimica Acta*, **359**(1-2):1–26.

IEM (2018). Utah ASOS Network, Iowa State University. URL `https://mesonet.agron.iastate.edu/request/download.phtml?network=UT_ASOS`.

Joliffe, I. and Stephenson, D. (2003). *Forecast Verification: A Practitioner's Guide in Atmospheric Science*. John Wiley & Sons.

Koren, I., Kaufman, Y. J., Rosenfeld, D., Remer, L. A., and Rudich, Y. (2005). Aerosol Invigoration and Restructuring of Atlantic Convective Clouds. *Geophysical Research Letters*, **32**(14):1–4.

Krehbiel, P., Hamlin, T., Harlin, J., Thomas, R., Rison, W., and Zhang, Y. (2001). Thunderstorm Observations with the Lightning Mapping Array. Technical report, New Mexico Institute of Mining and Technology, Socorro, New Mexico, USA.

Krider, E. P., Weidman, C. D., and Noggle, R. C. (1977). The Electric Fields Produced by Lightning Stepped Leaders. *Journal of Geophysical Research*, **82**(6):951–960.

Kumjian, M. R. (2013). Principles and Applications of Dual-Polarization Weather Radar. Part I: Description of the Polarimetric Radar Variables. *Journal of Operational Meteorology*, **1**(19):226–242.

Larsen, H. R. and Stansbury, E. J. (1974). Association of Lightning Flashes with Precipitation Cores Extending to Height 7 km. *Journal of Atmospheric and Terrestrial Physics*, **36**(9):1547–1553.

Mason, B. J. (1953). On the Generation of Charge Associated with Graupel Formation in Thunderstorms. *Quarterly Journal of the Royal Meteorological Society*, **79**(342):501–509.

Meischner, P. (2005). *Weather Radar Principles and Advanced Applications*. Springer Science & Business Media.

Nava, O. (2018). Reanalysis of the Travis (2015) OUI Calculation for 45th Weather Squadron. Technical report, Air Force Institute of Technology, Wright-Patterson AFB, Ohio, USA.

New Mexico Tech (2018). New Mexico Tech Lightning Homepage. URL `http://lightning.nmt.edu/`.

NLSI (2018). Lightning Safety. URL `http://lightningsafety.com/`.

NOAA (2018a). Interactive Radar Data Map. URL `https://gis.ncdc.noaa.gov/maps/ncei/radar`.

NOAA (2018b). National Centers for Environmental Information. URL `https://www.ncdc.noaa.gov/`.

NWS (2017). Dual Polarization Radar. URL `https://www.weather.gov/bmx/radar_dualpol`.

NWS (2018). Radar Operations Center. URL `https://www.roc.noaa.gov/WSR88D/`.

Olsen, S. (2018). Forecasting Lightning Initiation Utilizing Dual-Polarization Radar Parameters over Washington, D.C. Master's thesis, Air Force Institute of Technology.

Patton, J. R. (2017). Using Radar-Derived Parameters to Develop Probabilistic Guidance for Lightning Cessation Within Isolated Convection Near Cape Canaveral, Florida. Master's thesis, Florida State University.

Petty, G. W. (2006). *A First Course in Atmospheric Radiation*. Sundog, second edition.

Proctor, D. E. (1981). VHF Radio Pictures of Cloud Flashes. *Journal of Geophysical Research*, **86**(80):4041–4071.

Rakov, V. A. and Uman, M. A. (2003). *Lightning: Physics and Effects*. Cambridge University Press.

Reynolds, S. E., Brook, M., and Gourley, M. F. (1957). Thunderstorm Charge Separation. *Journal of Meteorology*, **14**(5):426–436.

Rison, W. (2018). Personal Correspondence.

Roeder, W. P. (2010). The Four Dimensional Lightning Surveillance System. In *Third Int. Lightning Meteorology Conf.*, pages 1–15.

Roeder, W. P. (2018). Personal Correspondence.

Roeder, W. P. and Pinder, C. S. (1998). Lightning forecasting techniques for Central Florida in support of Americas space program. In *16th Conference on Weather Analysis and Forecasting*.

Rogers, R. R. and Yau, M. K. (1989). *A Short Course in Cloud Physics*. Third edition.

Saunders, C. (2008). Charge Separation Mechanisms in Clouds. *Space Science Reviews*, **137**(1-4):335–353.

Singh, K. and Xie, M. (2008). Bootstrap: A Statistical Method. Technical report.

Takahashi, T. (1978). Riming Electrification as a Charge Generation Mechanism in Thunderstorms. *Journal of the Atmospheric Sciences*, **35**(8):1536–1548.

The University of Oklahoma (2005). Lightning Mapping Arrays. URL `http://weather.ou.edu/~nwilson/lma.html`.

Thomas, R. J., Krehbiel, P. R., Rison, W., Hunyady, S. J., Winn, W. P., Hamlin, T., and Harlin, J. (2004). Accuracy of the Lightning Mapping Array. *Journal of Geophysical Research D: Atmospheres*, **109**(14):1–34.

Thurmond, K. (2014). Operational Cloud-to-Ground Lightning Initiation Forecasting Utilizing S-Band Dual-Polarization Radar. Master's thesis, Air Force Institute of Technology.

Travis, A. (2015). Utilizing Four Dimensional Lightning and Dual-Polarization Radar to Develop Lightning Initiation Forecast Guidance. Master's thesis, Air Force Institute of Technology.

Uman, M. A. (2001). *The Lightning Discharge*. Dover Publications, Mineola, New York, USA.

U.S. DoL (2018). Bureau of Labor Statistics. URL `https://www.bls.gov/`.

Vaisala (2018a). AviMet LLWAS. URL `https://www.vaisala.com/en/products/systems/avimetr-low-level-wind-shear-alert-system-llwas`.

Vaisala (2018b). Vaisala NLDN. URL `https://www.vaisala.com/en/products/data-subscriptions-and-reports/data-sets/nldn`.

Wallace, J. M. and Hobbs, P. V. (2006). *Atmospheric Science: An Introductory Survey*. Elsevier, second edition.

84

Whiton, R. C., Smith, P. L., Bigler, S. G., Wilk, K. E., and Harbuck, A. C. (1998). History of Operational Use of Weather Radar by U.S. Weather Services. Part II: Development of Operational Doppler Weather Radars. *Weather and Forecasting*, **13**(2):244–252.

Woodard, C. J., Carey, L. D., Petersen, W. A., and Roeder, W. P. (2012). Operational Lightning Forecasting Technique Development and Testing Utilizing C-Band Dual-Polarimetric Radar. *Journal of Operational Meteorology*, **13**(6):79–102.

Yang, Y. H. and King, P. (2010). Investigating the Potential of Using Radar Echo Reflectivity to Nowcast Cloud-to-Ground Lightning Initiation over Southern Ontario. *Weather and Forecasting*, **25**(4):1235–1248.

Vita

First Lieutenant Daniel Katuzienski was born into a USAF family in Okinawa, Japan, but primarily grew up in Yorktown, Virginia. After graduating Tabb High School in 2011 in Yorktown, Virginia, he attended Virginia Polytechnic Institute and State University in Blacksburg, Virginia. He enrolled into the Air Force Reserve Officer Training Corps, Detachment 875, and graduated Magna Cum Laude with a Bachelor of Science Degree in Meteorology with a minor in Leadership Studies. Upon graduation in May 2015, he was commissioned as a Second Lieutenant in the USAF.

Lieutenant Katuzienski's first assignment was at the 28th Operational Weather Squadron, Shaw AFB, South Carolina. There he served in all forecasting positions before rising to the position of Senior Duty Officer. During this assignment, Lieutenant Katuzienski supported Operations INHERENT RESOLVE and ENDURING FREEDOM over Southwest Asia and Afghanistan, overseeing an operations center that created 45,000 weather forecasts that enabled more than 25,000 combat sorties.

In August 2017, Lieutenant Katuzienski entered the Graduate School of Engineering and Management at the Air Force Institute of Technology, Wright-Patterson AFB, Ohio to obtain a Master's Degree in Atmospheric Science with a specialization in Radar Meteorology. Upon graduation, he will be assigned to the 2nd Combat Weather Systems Squadron at Hurlburt Field, Florida, to be a Flight Commander.

1. REPORT DATE *(DD–MM–YYYY)*	2. REPORT TYPE	3. DATES COVERED *(From — To)*
02–26–2019	Master's Thesis	Aug 2017 — Mar 2019

4. TITLE AND SUBTITLE	5a. CONTRACT NUMBER
COMPARING DUAL-POLARIZATION RADAR LIGHTNING FORECAST METHODS ACROSS SOUTHWEST UTAH	
	5b. GRANT NUMBER
	5c. PROGRAM ELEMENT NUMBER

6. AUTHOR(S)	5d. PROJECT NUMBER
Katuzienski, Daniel Owen, 1st Lt, USAF	
	5e. TASK NUMBER
	5f. WORK UNIT NUMBER

7. PERFORMING ORGANIZATION NAME(S) AND ADDRESS(ES)	8. PERFORMING ORGANIZATION REPORT NUMBER
Air Force Institute of Technology Graduate School of Engineering and Management (AFIT/EN) 2950 Hobson Way WPAFB OH 45433-7765	AFIT-ENP-MS-19-M-083

9. SPONSORING / MONITORING AGENCY NAME(S) AND ADDRESS(ES)	10. SPONSOR/MONITOR'S ACRONYM(S)
45th Weather Squadron 1201 Edward H. White Ste. C-129 Patrick AFB, FL 32925 COMM 321-853-8410 Email: William.Roeder@us.af.mil	45 WS
	11. SPONSOR/MONITOR'S REPORT NUMBER(S)

12. DISTRIBUTION / AVAILABILITY STATEMENT

DISTRIBUTION STATEMENT A:
APPROVED FOR PUBLIC RELEASE; DISTRIBUTION UNLIMITED.

13. SUPPLEMENTARY NOTES

14. ABSTRACT

This study tests two lightning initiation prediction methods developed for the Cape Canaveral Air Force Station (CCAFS) and Kennedy Space Center (KSC) areas in the new geographical region of Utah. One method is composed of Dual-Polarization (DP) radar variables and the other uses non-DP radar parameters. The non-DP method, from Gremillion and Orville (1999), is reflectivity $(Z) \geq 40$ dBZ for two consecutive volume scans at the -10°C thermal height. The DP method, from Travis (2015), is $Z \geq 36.5$ dBZ with differential reflectivity $(Z_{DR}) \geq 0.31$ dB at the -10°C thermal height. Performance metrics, lead times, and Z and Z_{DR} optimizations show that traditional radar parameters for lightning initiation are geographically robust and that DP lightning prediction is not geographically robust. This result suggests that radar/lightning optimizations must be completed regionally to best forecast lightning. Additional results conclude that Z is the determining factor for Utah lightning initiation and that Z_{DR} is negligible.

15. SUBJECT TERMS

Lightning Initiation, Lightning Mapping Array, Lightning Prediction, Dual-Polarization Radar

16. SECURITY CLASSIFICATION OF:			17. LIMITATION OF ABSTRACT	18. NUMBER OF PAGES	19a. NAME OF RESPONSIBLE PERSON
a. REPORT	b. ABSTRACT	c. THIS PAGE			Maj Omar Nava, AFIT/ENP
U	U	U	U	86	19b. TELEPHONE NUMBER *(include area code)* (937) 255-3636, x4518; Omar.Nava@afit.edu